ACCEPTED FOR PUBLICATION IN APJS
Preprint typeset using LaTeX style emulateapj v. 01/23/15

POWERFUL ACTIVITY IN THE BRIGHT AGES. I. A VISIBLE/IR SURVEY OF HIGH REDSHIFT 3C RADIO GALAXIES AND QUASARS

B. HILBERT[1], M. CHIABERGE[1,2], J. P. KOTYLA[1], G. R. TREMBLAY[3], C. STANGHELLINI[4], W. B. SPARKS[1], S. BAUM[5,6], A. CAPETTI[7], F. D. MACCHETTO[1], G. K. MILEY[8], C. P. O'DEA[5,6], E. S. PERLMAN[9], A. C. QUILLEN[6]

Accepted for Publication in ApJS

ABSTRACT

We present new rest frame UV and visible observations of 22 high-z ($1 < z < 2.5$) 3C radio galaxies and QSOs obtained with the Hubble Space Telescope's (HST) Wide Field Camera 3 (WFC3) instrument. Using a custom data reduction strategy in order to assure the removal of cosmic rays, persistence signal, and other data artifacts, we have produced high-quality science-ready images of the targets and their local environments. We observe targets with regions of UV emission suggestive of active star formation. In addition, several targets exhibit highly distorted host galaxy morphologies in the rest frame visible images. Photometric analyses reveals that brighter QSOs tend to be generally redder than their dimmer counterparts. Using emission line fluxes from the literature, we estimate that emission line contamination is relatively small in the rest frame UV images for the QSOs. Using archival VLA data, we have also created radio map overlays for each of our targets, allowing for analysis of the optical and radio axes alignment.

Subject headings: galaxies: active – quasars: emission lines – quasars: general

1. INTRODUCTION

In the epoch between redshifts 1 and 2, the Universe was in a period of rampant star formation, AGN phenomena were 1000 times more common than at the present time, and there were many powerful, massive quasars and radio galaxies. There are many questions about the behavior and evolution of these dynamic objects and processes during these "Bright Ages". What fraction of these objects are in clusters or active mergers? How does the AGN affect star formation in its local environment? Do radio synchrotron jets quench or trigger star formation?

In order to provide a large database for studies aimed at addressing all of these questions, we have used the WFC3 instrument to obtain multiband optical and IR images of a set of $1< z <2.5$ radio galaxies and QSOs in the 3CR catalog (Spinrad et al. 1985). The 3CR catalog is unbiased with respect to orientation effects and contains the most powerful radio sources at any given redshift, allowing us a view of the behaviors of the progenitors of some of the most massive, dominant cluster elliptical galaxies. From these data, we can begin to address many of the fundamental questions of galaxy and cluster behavior at this exciting time in the Universe's history, including details of star formation rates and cluster environments and the prevalence of mergers.

[1] Space Telescope Science Institute, 3700 San Martin Drive, Baltimore, MD 21218
[2] Center for Astrophysical Sciences, Johns Hopkins University, 3400 N. Charles Street, Baltimore, MD 21218, USA
[3] Yale University, Department of Astronomy and Yale Center for Astronomy and Astrophysics, 52 Hillhouse Ave, New Haven, CT 06511
[4] INAF - Istituto di Radioastronomia, Via P. Gobetti, 101 40129 Bologna, Italy
[5] University of Manitoba, Dept of Physics and Astronomy, 66 Chancellors Cir., Winnipeg, MB R3T 2N2 Canada
[6] Rochester Institute of Technology, School of Physics & Astronomy, 84 Lomb Memorial Dr., Rochester, NY, 14623, USA
[7] Osservatorio Astronomico de Torino, Corso Savona, 10024 Moncalieri TO, Italy
[8] Universiteit Leiden, Rapenburg 70, 2311 EZ Leiden, Netherlands
[9] Florida Institute of Technology, 150 W University Blvd, Melbourne, FL 32901

Here we present our calibrated data, along with qualitative descriptions of the features in the observations, as well as initial photometric and emission line analyses of the objects.

Combined with data from previous SNAPSHOTS of 3C objects at lower redshifts (e.g. Madrid et al. (2006); Tremblay et al. (2009)) we can look for evolutionary trends over long timescales, including AGN and host galaxy interaction from z∼2 to today. Scientific results from these data are presented in a series of papers e.g. Chiaberge et al. (2015), Kotyla et al. (2015, in preparation), and Chaiberge et al. (2016, in preparation).

2. THE OBSERVED SAMPLE

We used WFC3 on board HST to obtain visible and near-IR images of our 3C targets under SNAPSHOT proposal 13023. These data were collected between December of 2012 and May 2013.

The sample definition is the revised 3C catalog as defined by (Bennett 1962a), (Bennett 1962b), (Spinrad et al. 1985). The 3CR catalog includes all radio sources with flux density at 178MHz $S_{178} > 9$Jy that are located at a latitude $|b| > 10°$. From these, we restricted our proposed target list to the 58 sources with $z > 1.0$. Over the course of Cycle 20, we obtained data for 22 of these objects, representing 38% of our proposed sample. Of these 22 objects, 12 are high-excitation narrow line radio galaxies (RGs) and 10 are QSOs. Observed targets are listed in table 1 along with some of their basic properties. These objects cover a range in redshift from 1.055 to 1.825, with the exception of 3C 257 at $z = 2.474$.

2.1. *Statistical properties of the observed sample*

The average completion rate for HST/WFC3 SNAPSHOT programs is currently (Cycle 20-21) $\sim 30\%$ (Workman et al. 2014). This is most likely due to the STScI policy that lowers the scheduling priority of targets belonging to programs that reach the 35% completion rate limit. As a result, our program was efficiently scheduled in the first part of the HST Cycle 20. Unfortunately, as soon as we reached the 35% limit, the observations stopped, and no other targets were scheduled after June 2013.

Our total of 22 observed objects represents a rather small fraction of the complete catalog of sources. This is particularly significant for statistical work, for example to firmly establish the fraction of objects that show specific properties and to derive important information on the nature of these radio sources. The STScI procedure for selecting a subset of sources from a snapshot proposal should not result in any bias in terms of source properties. Nevertheless, it is very important to test that the observed sample is representative of the entire population of objects belonging to the 3CR. In Fig. 2 we show the distribution of total radio power at 178MHz (left panel) and redshift (right panel) for the whole 3CR sample with $z > 1$ (in red) and for our observed sub-sample (in yellow). Visually, the yellow and red histograms appear to be similar. In fact, the Kolmogorov-Smirnov test shows that we cannot reject the null hypothesis that the observed and the full sample follow the same redshift and radio power distributions. The p-values are $p = 0.998$ and $p = 0.995$ for the radio power and redshift distributions, respectively. The statistical test is performed using the *R* function *ks.boot* included in the *Matching* package (Sekhon 2011). This function performs a bootstrap version of the K-S test that is useful when statistical ties are present in the samples, as it is in our case. However, an identical result is returned by the classical KS test (*ks.test*).

While this analysis does not prove that the observed and original distributions are the same, it provides support to the idea that our sample of 22 objects is a good representation of the original 3CR catalog at $z > 1$. However, note that with only 22 observed objects the statistical accuracy is significantly reduced (by a factor of ~ 2, assuming the binomial statistics and depending on the resulting object fraction) compared to the original sample. For example, if we observed that 70% of our objects display a specific property (e.g. the source is a member of a cluster of galaxies, the source is associated with a host galaxy brighter than a certain magnitude, etc.), we would not not be able to statistically establish whether our sample is different from any (larger) comparison sample that shows only 50% of objects associated with clusters. Instead, this would be possible if at least 77% of the full sample was observed. A higher level of statistical accuracy is clearly very important for a number of tasks, e.g. testing unification scenarios, comparing radio-loud and radio-quiet AGNs, establishing differences between inactive and active galaxies, etc.

2.2. *HST Observation Strategy*

Table 1 lists details of the HST data that have been collected for this analysis. We imaged each object with both the UVIS and IR channels of WFC3, through the filters which cover the highest DQE spectral regions of those channels. See the WFC3 Instrument Handbook (Dressel et al. 2014) for more technical details on the two channels within WFC3.

UVIS observations were made using the F606W filter, which has a pivot wavelength of 588.7 nm and a width of 218.2 nm. The field of view in the UVIS channel is 162" x 162" at a resolution of 0.04" per pixel. For each object, we collected 2 images with equal exposure times and a 2.4" pointing offset between one another, in order to enable cosmic ray rejection and to cover the 1.2" gap between the two UVIS CCDs. For QSO targets, we also collected a 30-second image, which will be used to facilitate PSF subtraction. This work will be described in a future paper.

The IR channel observing strategy was similar. Two observations of each object were made through the F140W filter (pivot wavelength 1392.2 nm, width 384 nm). These observations covered a 123" x 136" field of view, at a resolution of 0.13" per pixel. For each observation, we used the SPARS50 sample sequence with 11 non-destructive detector readouts, translating into an exposure time of 249 seconds. We also imposed a 1.25" dither between the two IR channel observations of each object.

3. DATA REDUCTION

In this section, we focus on the data reduction strategies and techniques we use to produce the highest-quality visible and near-IR images for each object. We customize the data reduction and image combination process, rather than using the drizzled images produced by the standard HST pipeline and available in the Mikulski Archive for Space Telescopes (MAST). Our calibrated and drizzled data are available at http://hz3c.stsci.edu, and will also be ingested into MAST as High Level Science Products (HLSP) available for download at http://archive.stsci.edu/hlsp/index.html.

For both the UVIS and IR channel data, we begin our custom data reduction routine with with the *flt* files output by the standard *calwf3* data reduction pipeline. The pipeline performs basic calibration steps on the raw data, including bias and dark current subtraction, linearity correction, flat fielding, and bad pixel masking. Additionally, for IR data *calwf3* identifies and removes cosmic ray effects. It also fits a line to the multiple signal values for each pixel, and outputs the pixel's signal rate in the *flt* file. For more details on the calibration steps performed by *calwf3*, see the WFC3 Data Handbook (Deustua et al. 2016). We also check to be sure that *calwf3* is run with the best available reference files for our data.

3.1. *UVIS Data*

Beginning with the *calwf3*-output *flt* images, we first correct charge transfer efficiency (CTE) effects in the files by running them through the CTE correction algorithm (Anderson & Bedin 2010). This correction models the details of how charge traps in the UVIS detector grab and release charge during the readout process. From this, the correction script is able to identify charge which was caught in charge traps during the detector readout, and return it to the proper pixels. This greatly reduces the magnitude of the CTE-induced charge trails in the original *flt* images. The resulting data are saved in *flc* files.

After the CTE correction is performed we are able to focus on cosmic ray rejection. Astrodrizzle, which is part of the Drizzlepac software package (Gonzaga et al. 2012), allows for identification and removal cosmic rays from WFC3 data, as well as the removal of the geometric distortion from the images. It also then combines the individual images into a final, clean image. Astrodrizzle eliminates cosmic rays by placing multiple images of the same section of sky onto the same pixel grid and then comparing the measured signals in each pixel through the stack of observations. If, for a given pixel, one image in the stack shows an anomalous signal compared to the mean of all the signals, Astrodrizzle will flag the anomalous signal as a cosmic ray hit.

However, with our data composed of only two dithered images per object, we only have two measures of the signal at any given point on the sky. Any location impacted by a cosmic ray in one image therefore leaves us with one good measure of the signal for that point on the sky, along with one bad measurement. In this situation, Astrodrizzle has no knowledge of which of the two measures is good and which is bad. The

TABLE 1
BASIC CHARACTERISTICS AND EXPOSURE TIMES OF OBSERVED OBJECTS.

3C Num	RA	Dec	z	F606W Exp Time (sec)	F140W Exp Time (sec)	S_{178MHz} (Jy)	Log L_{178MHz} (erg/sec/Hz)
				Radio Galaxies			
3C 210	8:58:10.0	+27:50:52	1.169	2 x 500	2 x 249.23	9.5	35.85
3C 230	9:51:58.8	-00:01:27	1.487	2 x 510	2 x 249.23	19.2	36.37
3C 255	11:19:25.2	-03:02:52	1.355	2 x 500	2 x 249.23	13.3	36.13
3C 257	11:23:09.2	+05:30.19	2.474	2 x 520	2 x 249.23	9.7	36.30
3C 297	14:17:24.0	-04:00:48	1.406	2 x 500	2 x 249.23	10.3[a]	36.05
3C 300.1	14:28:31.3	-01:24:08	1.159	2 x 510	2 x 249.23	10.1	35.87
3C 305.1	14:47:09.5	+76:56:22	1.132	2 x 520	2 x 249.23	4.6	35.50
3C 322	15:35:01.2	+55:36:53	1.168	2 x 530	2 x 249.23	10.2	36.19
3C 324	15:49:48.9	+21:25:38	1.206	2 x 490	2 x 249.23	13.6	36.04
3C 326.1	15:56:10.1	+20:04:20	1.825	2 x 500	2 x 249.23	9.0	36.19
3C 356	17:24:19.0	+50:57:40	1.079	2 x 348 + 664	2 x 249.23	11.3	35.85
3C 454.1	22:50:32.9	+71:29:19	1.841	2 x 500	2 x 249.23	10.2	36.25
				QSOs			
3C 68.1	02:32:28.9	+34:23:47	1.238	2 x 550 + 30	2 x 249.23	12.1	36.01
3C 186	07:44:17.4	+37:53:17	1.069	2 x 550 + 30	2 x 249.23	13.0	35.90
3C 208	08:53:08.6	+13:52:55	1.112	2 x 550 + 30	2 x 249.23	17.0	36.06
3C 220.2	09:30:33.5	+36:01:24	1.157	2 x 550 + 30	2 x 249.23	8.6	35.80
3C 268.4	12:09:13.6	+43:39:21	1.402	2 x 550 + 30	2 x 249.23	9.5	36.01
3C 270.1	12:20:33.9	+33:43:12	1.528	2 x 550 + 30	2 x 249.23	12.7	36.21
3C 287	13:30:37.7	+25:09:11	1.055	2 x 550 + 30	2 x 249.23	16.0	35.98
3C 298	14:19:08.2	+06:28:35	1.438	2 x 550 + 30	2 x 249.23	47.1	36.73
3C 418	20:38:37.0	+51:19:13	1.686	2 x 500	2 x 249.23	11.9	36.26
3C 432	21:22:46.3	+17:04:38	1.785	2 x 550 + 30	2 x 249.23	12.5	36.32

[a] Radio flux value from (Kellermann et al. 1969).

traditional way to deal with this situation when combining images with Astrodrizzle is simply to assume that the lower of the two values is the uncontaminated signal, and to use that value in the final combined image. This limits the accuracy of the counts measured in the resulting combined image.

Instead, we attempt to recover some of the sky values in CR-contaminated pixels prior to combining images with Astrodrizzle. We use the Python version of LA Cosmic (van Dokkum 2001), cosmics.py, to identify and remove cosmic rays in our images. LA Cosmic identifies cosmic rays by using a variation of Laplacian edge detection, and can distinguish between cosmic rays and undersampled PSFs. For more details, see van Dokkum (2001). While this method is effective at locating cosmic rays within the data, we note that it replaces the signal values in the cosmic ray-impacted pixels with extrapolated counts from the surrounding pixels. It therefore introduces larger uncertainties in the recovered pixels compared to the use of a method such as Astrodrizzle for cosmic ray correction.

We run LA Cosmic on each individual *flc* file, using a set of conservative parameters to ensure that no signal is mistakenly removed from the astronomical sources. These parameters include a sigclip value of 5, sigfrac of 0.85, and objlim of 5. This run of LA Cosmic (hereafter Run 1) identifies the most obvious cosmic rays in each image, and replaces each impacted pixel with the median value of the surrounding good pixels.

We then run LA Cosmic a second time (Run 2) on the original *flc* file using more stringent parameters: sigclip value of 4.5, sigfrac of 0.65, and objlim of 2. The motivation for this is to improve the data quality in the areas of sky covered by the inter-chip gap in each of the original input images. The width of the inter-chip gap is approximately $1.2''$, while the dither between our two observations is roughly twice as large. With the inter-chip gap falling on a different area of the sky in each of the two exposures, when combining the images we create two $1.2''$ wide strips where the sky was only imaged once. Any cosmic rays impacting within these strips leave us with no uncontaminated measurements of the signal in that location.

We extract these regions from the clean *flc* obtained after Run 2 and insert them in the appropriate position of the *flc* file obtained after Run 1. Correcting a significant fraction of the cosmic ray population with LA Cosmic then allows Astrodrizzle to use 2 measures of the signal during image combination for many of the cosmic ray-impacted pixels.

After these initial cosmic ray correction steps, we use Astrodrizzle to remove residual cosmic rays and geometric distortion, to align, and combine the two individual images for each object into a final image. Final images were rotated into a north-up and east-left orientation.

Even after the previous cosmic ray correction steps, some residual cosmic rays in the drizzled images are still present. This is mainly due to the fact that two dither-points are not always sufficient to provide a fully clean image. This happens for two reasons: i) if two cosmic rays cover the same area of sky in both images, and ii) for particularly bright cosmic rays, the rejection algorithm in Astrodrizzle may not work perfectly, for reasons that are not completely understood but that most likely depend on the specific settings of that task and on the image noise level. We remove these residual cosmic rays using a custom procedure. First, we make a mask that includes pixels showing significant flux excess compared to the surrounding pixels. These are identified by a simple algorithm that compares each drizzled image with both the difference and the ratio of the original two images. The marked

pixels in the mask are then grown using a Gaussian kernel of appropriate FWHM (generally ~ 1 pixel), in order to fix a slightly larger area. This is important because these residual cosmic rays appear much more smoothed in the drizzled image than in the original FLT files, and while the brightest pixels are easily identified with this procedure, the adjacent fainter external pixels might not be correctly removed.

3.2. *IR Data*

The data reduction process for the IR channel data is relatively simpler than that for the UVIS data, due to the fact that the multiple non-destructive detector readouts within each observation allowed for easy cosmic ray identification and removal within the *calwf3* data reduction pipeline.

The first effect we deal with is persistence. This is an afterimage observed in pixels which in previous exposures were subjected to high flux levels. See Long (2011) for more details on persistence. Our goal is to remove any persistence signal present in our data, in order to avoid contaminating later photometry.

We begin by retrieving the persistence masks and persistence-corrected *flt* files of our observations from MAST. These files have had the persistence signal modeled and subtracted from them, following the model described in section 8.3 of version 4.0 of the WFC3 Data Handbook (Deustua et al. 2016), and are therefore different from the standard *flt* files available in the archive. Examination of these persistence masks reveals that for most objects there is no appreciable persistence contamination from prior observations. However, in some cases we do fall victim to self-persistence, where the bright sources in our initial exposure induced persistence in the following image. While the $1.25''$ (approximately 10-pixel) dither between observations is large enough that self-persistence from the central object is shifted outside of the object in the second image, there are cases where the shift results in this persistence signal appearing close to surrounding objects of interest. An example is shown in figure 3, where the panel on the left shows signal due to self-persistence inside the red circles. In the panel on the right, the persistence has been removed using the persistence model.

After careful examination of the persistence-corrected *flt* files from MAST, we chose to use these files for our subsequent analyses.

The next step in our data reduction is to remove the geometric distortion from all of the *flt* files, and to combine the two images for each object into a final IR image. We use Astrodrizzle to accomplish both of these steps.

We then use Tweakreg (also part of the Drizzlepac software package) to align this final image to the same world coordinate system present in the corresponding UVIS-channel drizzled image.

At this point it is possible to overlay the UVIS and IR image for a particular object and compare the morphology and brightness in the two observation bands.

4. PHOTOMETRY

Photometric analysis of the objects in our images is performed using SExtractor (Bertin&Arnouts 1996). Our strategy is to use the IR images for object identification and aperture definition. The resulting catalogs are then used for the photometry on both the IR and UVIS images. The motivation for this strategy lies in the fact that our UVIS data, which have an effective wavelength of roughly 6000 Å, are capturing UV rest frame photons for our targets at $z > 1$. These data are therefore biased towards showing irregularly shaped star forming regions rather than the entire galaxies, whose rest frame optical emission has been shifted into the wavelength range covered by our IR data. This means that many sources present in the IR data appear at a very low signal level, not at all, or with a significantly different morphology in the UVIS data. This renders the UVIS images unsuitable for aperture definition.

For example, the left panel of fig 4 shows that 3C 324 appears as an extended source stretching primarily east-west. However the corresponding UVIS image, seen in the right panel, reveals appreciable signal only in several distinct star forming regions within the host galaxy.

By basing the aperture used in the UVIS image on that defined within the IR image, we are sure to measure the total UVIS signal associated with 3C 324, rather than having SExtractor erroneously treat each star forming region as a separate object.

We therefore perform our photometry in two steps. First, using SExtractor in MAG_BEST mode, we obtain measurements of each target's flux in the IR data. In this mode, SExtractor determines the best elliptical aperture to use, and measures the flux inside that aperture. As an ancillary output, we have SExtractor calculate $R_{.9}$, the radius of a circle which would encompass 90% of the target's light.

We then use $R_{.9}$ as the basis of the UVIS photometry for the target. Testing on real and simulated sources of varying morphologies reveals that using a circular aperture which is 20% larger than $R_{.9}$ results in the full recovery of all of the object's flux in the UVIS image.

The photometry results are then corrected for galactic absorption and converted into AB magnitudes using the zeropoints provided by the WFC3 team.

Table 2 lists the resulting AB magnitudes and uncertainties for all of our targets. Note that in this paper we focus only on the results for our target 3CR sources rather than all of the objects in each image.

4.1. *Emission Line Contamination*

In addition to the broadband photometry results above, we are also interested in the amount of emission line contamination in the measured fluxes of our objects. Depending on the redshift of a particular target, it is possible to have flux from any of a series of emission lines shifted into the bandpasses of the F606W and F140W filters used to collect our data. As an example, Figure 5 shows a median composite QSO spectrum from Vanden Berk (2001) which we have redshifted to z=1.41 (e.g. similar to our target 3C 268.4) for illustrative purposes, with our filter bandpasses overlaid. In this case, we see that the FeII and MgII emission lines are present within the F606W bandpass, and that the [OIII] and Hβ lines are present at opposite ends of the F140W bandpass. This suggests that flux from these four emission lines may be contributing to the total fluxes we calculated in our photometry calculations. Table 3 lists the emission lines which fall within our two filter bandpasses for all of our targets. We base these lists on the redshift of each target, as well as the rest frame wavelength of each emission line feature.

For each of our targets, we search the literature for published fluxes for emission lines which fall within the F140W and F606W bandpasses. We input each flux value into the WFC3 Exposure Time Calculator (ETC) to estimate the measured count rate that emission line would produce on the relevant WFC3 detector. We then compare these predicted emis-

TABLE 2
AB MAGNITUDES FOR ALL OBJECTS, CORRECTED FOR GALACTIC ABSORPTION.

Target	F606W Mag	F140W Mag
Radio Galaxies		
3C210	21.770 ± 0.035	19.790 ± 0.005
3C230	22.386 ± 0.040	19.971 ± 0.016
3C255	23.356 ± 0.082	20.755 ± 0.009
3C257	24.422 ± 0.221	21.404 ± 0.018
3C297	21.855 ± 0.033	19.377 ± 0.003
3C300.1	22.508 ± 0.072	19.837 ± 0.005
3C305.1	21.330 ± 0.023	19.446 ± 0.003
3C322	23.491 ± 0.074	20.584 ± 0.006
3C324	22.233 ± 0.040	19.688 ± 0.004
3C326.1	25.140 ± 0.251	22.197 ± 0.033
3C356	22.032 ± 0.030	19.762 ± 0.004
3C454.1	22.497 ± 0.124	19.577 ± 0.003
QSOs		
3C68.1	19.474 ± 0.002	17.299 ± 0.001
3C186	17.747 ± 0.001	17.367 ± 0.001
3C208	17.829 ± 0.001	17.027 ± 0.001
3C220.2	18.451 ± 0.001	17.705 ± 0.001
3C268.4	17.915 ± 0.001	16.548 ± 0.001
3C270.1	18.531 ± 0.001	17.795 ± 0.001
3C287	18.176 ± 0.001	17.818 ± 0.001
3C298	17.276 ± 0.001	15.981 ± 0.001
3C418	17.798 ± 0.003	17.224 ± 0.001
3C432	18.163 ± 0.001	18.137 ± 0.001

TABLE 3
EMISSION LINES IN OUR TARGET IMAGES.

3C Num	Em. Lines within UVIS bandpass	Em. Lines within IR bandpass
Radio Galaxies		
3C 210	MgII	Hα
3C 230	MgII	Hβ, [OIII]
3C 255	MgII	Hα
3C 257	CIII]	none
3C 297	MgII	Hα, [OIII]
3C 300.1	MgII	Hα
3C 305.1	MgII	Hα
3C 322	MgII	Hα
3C 324	MgII	Hα
3C 326.1	CIII]	Hβ, [OIII]
3C 356	MgII	Hα
3C 454.1	CIII]	Hβ, [OIII]
QSOs		
3C 68.1	FeII, MgII	Hα
3C 186	MgII	Hα
3C 208	MgII	Hα
3C 220.2	MgII	Hα
3C 268.4	FeII, MgII	Hα, [OIII]
3C 270.1	CIII], FeII, MgII	Hβ, [OIII]
3C 287	MgII	Hα
3C 298	FeII, MgII	[OIII]
3C 418	CIII], FeII	Hβ, [OIII]
3C 432	CIII], FeII	Hβ, [OIII]

NOTE. — Here we list the emission lines which fall within the filter bandpasses for all targets. This information is based on the redshifts of the targets as well as the rest frame wavelengths of the emission lines. The rest frame wavelengths of the emission lines are: MgII 2798Å, CIII] 1909Å, FeII 2200-2800Å, [OIII] 5007Å, Hα 6563Å, Hβ 4861Å.

sion line signals with our broadband photometry results to obtain a measure of the emission line contamination.

Table 4 shows the results, where each row of the table contains the contamination estimate for a single emission line in one of our targets. We find published emission line fluxes for a limited set of targets and emission lines. Most fluxes are from data contained in the Sloan Digital Sky Survey's Data Release 9 (Ahn et al. 2012), and are for emission lines present within the F606W bandpass for the QSO targets. We find fluxes for only two emission lines in radio galaxy targets. The first is the flux of the MgII2798 emission line within the F606W bandpass for 3C 356 from Lacy & Rawlings (1994). The only measured flux for an emission line in the F140W bandpass comes from Jackson & Rawlings (1997), for the [OIII]5007 line in 3C 297.

All emission line fluxes from the literature were measured using $3''$ apertures, with the exception of the $2''$ aperture used by Lacy & Rawlings (1994) for the 3C 356 observations. Examining a single exposure taken with a $3''$ aperture, Lacy & Rawlings (1994) find that the only emission line for which the signal extends beyond their $2''$ aperture is the [OII] 3727 line.

While these apertures do not exactly match our broadband photometry apertures, we are confident that our apertures capture all of the broadband QSO and RG flux. In addition, we believe that the $3''$ emission line apertures captured all of the emission line flux.

For the QSOs the $3''$ apertures should have captured all of the emission line flux because the dominant part of the MgII line is from the broad component, which is emitted within the point source. For the radio galaxy emission line fluxes, in agreement with the findings of Lacy & Rawlings (1994), we find that 3C 356 is smaller than $1''$ in the rest frame UV image, indicating that a $3''$ aperture should capture all of the flux. The galaxy associated with 3C 297 is larger than $3''$. However, at the distance of 3C 297, $3''$ corresponds to about 25 kpc. The typical size of the narrow line region (NLR) in radio galaxies is of order 10kpc (e.g. (Baum & Heckman 1989)). Therefore we are confident that a $3''$ aperture should contain most if not all of the emission line flux for this case as well.

Using these signals as inputs to the ETC, we find that no single emission line contributes more than 2.6% of an object's total signal.

We attempt to estimate contaminations for a larger set of emission lines, using typical emission line ratios (e.g. (Netzer 1990)) to estimate fluxes for emission lines without published fluxes. However, this method does not account for the dust obscuration of our targets, and leads to highly uncertain results.

4.2. *Radio Observations*

In addition to the visible/IR observations, we also make use of archival VLA radio observations of our objects. The combination of the HST and VLA data allows us to examine the relative positions of radio lobes and star forming regions.

Over the last few decades, 3CR radio sources have been target sources for many VLA projects, and the NRAO VLA archive contains many useful data sets.

Radio data from the NRAO VLA archive have been selected on the basis of the following criteria: a) longer integration time to increase general sensitivity; b) frequency and array configuration to match the angular resolution of the visible/IR images as much as possible. Different frequencies on the same target have been selected, when possible, to obtain the spectral index information. Table 5 lists the basic information on the radio data selected.

TABLE 4
EMISSION LINE INFORMATION FOR OUR TARGETS

3C Num	Filter	Em. Lines within bandpass	Em. Line Flux $erg/s/cm^2$ $\times 10^{-15}$	Em. Line Ref	Em. Line Contamination	Other Em. Lines Potentially Present
			Radio Galaxies			
3C 297	*F140W*	*[OIII]5007*	10.3	[a]	0.03%	$H\alpha$
3C 356	F606W	MgII2798	17	[b]	1.6%	-
			QSOs			
3C 186	F606W	MgII2798	12.6	[c]	2.4%	-
3C 208	F606W	MgII2798	13.4	[c]	2.6%	-
3C 220.2	F606W	MgII2798	6.9	[c]	2.4%	-
3C 268.4	F606W	MgII2798	9.6	[c]	2.1%	FeII2200-2800
3C 270.1	F606W	MgII2798	6.0	[c]	1.7%	FeII2200-2800
3C 270.1	F606W	CIII]1909	5.4	[c]	1.3%	FeII2200-2800
3C 287	F606W	MgII2798	3.2	[c]	0.8%	-
3C 298	F606W	MgII2798	19.8	[c]	2.5%	FeII2200-2800

NOTE. — The second column lists the filter bandpass within which the emission line appears, and the third column lists the emission line and corresponding rest wavelength. The fluxes listed in the fourth column are measured from SDSS (Ahn et al. 2012) with the exception of the [OIII] line in 3C 297 and the MgII line in 3C 356. The sixth column lists the percentage of signal in our observations which could come from these emission lines. The rightmost column lists other emission lines which are present within the bandpasses of our observations, but for which we do not have measured flux values, and therefore no contamination estimates. The only F140W emission line for which we have a measured flux is the [OIII] line for 3C 297, indicated with italics. All other emission line fluxes are for contamination in the F606W observations.

[a] Flux used to estimate emission line signals from (Jackson & Rawlings 1997). The stated uncertainty in this flux is 15-25%, which has a small effect on our calculated contamination percentage.

[b] Flux used to estimate emission line contamination from Lacy & Rawlings (1994). We also note a similar flux of $13\times10^{-15} erg/s/cm^{-2}$ from Cimatti et al. (1997).

[c] Emission line flux from SDSS (Ahn et al. 2012).

The selected VLA archive data were retrieved from the online database in FITS format and loaded into the NRAO Astronomical Image Processing System (AIPS). Data reduction followed the standard procedure. The absolute flux density scale have been determined with the observations of a primary calibrator (3C286, 3C48 or 3C147). AIPS includes values of the flux densities of the primary calibrators taken during several years. We used the values closer in time to the target source observations (task SETJY). The flux density scale used at the VLA up to 15 GHz, for these archival data, is based on the flux density of 3C295 determined by Baars et al. (1977). At frequencies above 15 GHz the flux density scale is based on observations and emission models for the planet Mars. Phase calibration has been performed using the phase calibrators available for each archive data set, closer to the targets.

Errors on the flux density due to the calibration procedure, unless differently indicated, are estimated to be 3% at 5/8.4GHz, and 5% at 15/22GHz.

After manual editing of bad fringe visibilities, iterations of phase self-calibration were performed to correct for antenna based errors, until the process converged to a stable solution (task CALIB), followed by a final step of amplitude and phase self-calibration, if the improvement of the r.m.s. on the final image was significant.

Imaging have been through a clean and restore algorithm (task IMAGR), with a suitable choice of fringe visibility weighting (ROBUST/UVBOX parameters) to get the best balance between angular resolution, sensitivity to the extended emission, r.m.s. on the images, then optimizing the comparison with the visible/IR images.

5. COLOR MAGNITUDE DIAGRAM

Figure 6 shows the color-magnitude diagram (CMD) produced from our photometry. The blue points show the results for the QSO targets, while the red points represent the RG targets.

We see that the QSOs are generally more blue than the RGs. This is expected as the bluer AGN spectrum dominates over the redder host galaxy spectrum in the QSOs.

3C 68.1 is the exception to this rule, with a color comparable to many of the RGs. Wilkes et al. (2013) measures an absorbing column density of $9.0\times10^{22} cm^{-2}$ for 3C 68.1. Brotherton et al. (1998) showed that the object is characterized by reddened polarized scattered light from the nucleus. Without reddening, the location of the 3C 68.1 point would move down and to the left (i.e. bluer and brighter), closer to the values for the other QSOs.

Among the RG targets, two of the three farthest targets, 3C 257 and 3C 326.1, are the reddest. Beyond that, the RGs show no clear color trends. Conversely, as a group the QSO targets appear to become more red as their brightness increases. In order to assure ourselves that this trend was not the result of the different redshifts of the sources, we produce a set of simulated QSO magnitudes and colors for comparison. We use the QSO1 template spectrum from (Polletta 2007), which was created by calculating the average spectrum from a set of 35 SDSS quasar spectra and rest frame IR data. We redshift and renormalize the template spectrum to match the redshift and F140W magnitude of each of our target QSOs. We then calculate the F606W magnitude for each object, and plot the calculated color versus the F140W magnitude as the black points in figure 6. Vertical dashed black lines connect each observed QSO color (in blue), with the model color (in black) for each object.

The color differences between the blue and black points

TABLE 5
VLA ARCHIVE RADIO DATA

Target	VLA code	freq.(GHz)	VLA conf.	obs. date	# vis.	FWHM(")	rms(uJy)
			Radio Galaxies				
3C210	AO230	4.86	B	19-Apr-2009	39754	1.21x1.02@-17°	100
3C230	AK403	8.44	A	27-Jul-1995	13845	0.32x0.23@-38°	70
3C255	AV157	8.44	A	22-Dec-1988	32643	0.29x0.23@20°	30
3C257	AV164	8.44	A	11-May-1990	62429	0.41x0.23@43°	30
3C297	AV164	8.44	A	10-May-1990	62452	0.44x0.29@37°	20
3C300.1	AK403	8.44	A	27-Jul-1995	37364	0.29x0.24@38°	50
3C305.1	AM141	14.94	A	18-Feb-1985	16987	0.17x0.10@-33°	250
3C322	AV133	4.86	A	16-Apr-1986	111530	0.49x0.29@85°	80
3C324	AB755	8.21	A	11-Jul-1995	472658	0.20x0.20	15
3C326.1	AV133	14.94	A	16-Apr-1986	73118	0.17x0.12@-69°	150
3C356	AF186	4.85	A	22-Apr-1990	334997	0.35x0.35	30
3C454.1	AM213	4.86	A	17-Aug-1987	80633	0.36x0.34@-90°	100
3C454.1	AM213	14.94	A	17-Aug-1987	119846	0.12x0.11@35°	150
			QSOs				
3C68.1	AB369	4.86	A	29-Mar-1986	678366	0.29x0.26@-3°	30
3C186	AA129	8.44	A	14-Sep-1991	8296	0.22x0.20@30°	100
3C208	AL280	8.44	A	13-Dec-1992	109850	0.20x0.20	40
3C220.2	AK403	8.44	A	27-Jul-1995	12493	0.25x0.25	40
3C268.4	AB796	8.46	A	07-Nov-1996	457566	0.18x0.17@-8°	30
3C270.1	AB796	8.46	A	07-Nov-1996	554306	0.18x0.18	40
3C287	AP263	8.44	A	02-Mar-1994	28434	0.26x0.21@75°	400
3C298	AA149	22.46	A	10-Nov-1992	15021	0.093x0.075@-33°	400
3C418	AM299	4.86	A	14-May-1990	247857	0.54x0.33@55°	700
3C432	AL280	8.44	A	13-Dec-1992	140375	0.23x0.20@-85°	40

NOTE. — VLA archive radio data. The second column from the left lists the project identification number of the observations. The third column from the right lists the number of fringe visibilities of the final dataset after flagging and calibration. Each visibility is a single data point of 2 antennas of the interferometer and has a 10 second integration time.

may imply that the spectra of our targets do not match the template spectrum we used to estimate the location of our QSOs in the CMD. A possible effect that might contribute to redden our sources is obscuration, as in the case of 3C68.1. However, even if reddening affects the flux measured in F606W more significantly than that in F140W, we would still expect to see a correlation between reddening and F140W magnitude (i.e. the redder the source, the fainter). Unless the brighter QSOs in the CMD are intrinsically brighter at a level sufficient to counter the obscuration effect in F140W, we do not believe that the presence of reddening is the correct interpretation. Another possible effect is the presence of a stronger emission line contamination in the redder filter in sources that are intrinsically brighter. We currently do not have enough information to distinguish which of these situations is the true cause. However, since the black dots span a narrow range in color, we can conclude that redshift alone has a very small effect in determining the location of the QSOs in the CMD plot.

6. NOTES ON INDIVIDUAL OBJECTS

In this section we give qualitative descriptions of the objects and environments in both the visible/IR images and the corresponding radio data, as well as notes on the alignment between the two. We look for the alignment effect (Miley & De Breuck 2008), where the radio signal falls along the same line as the optical continuum emissions. We note potential regions of active star formation based on the presence of concentrated areas of UVIS emission in our observations. We also note that Chiaberge et al. (2015) find that all RGs in this sample show signs of recent merger activity, with the exception of 3C 230, where the host galaxy is not visible. Figures 7 through 50 show the visible and IR observations for all targets, while figures 51 through 54 show the enlarged central portions of the visible and IR observations with radio map overlays.

The uncertainties in the world coordinate systems (WCS) of the VLA data are relatively large compared to the visible/IR data. For sources containing a radio core, we shifted the radio data in order to align the radio core with the visible/IR core. The magnitude of these shifts were typically less than $1''$. From this we assume that the positional uncertainty for the sources with no radio cores is also under $1''$.

6.1. *Radio Galaxies*

6.1.1. *3C 210 (z=1.169)*

3C 210 is the eponymous member of the 3C 210 galaxy cluster (Stanford et al. 2002). The cluster appears in our IR image as an overdense region of red galaxies. The host of 3C210 is clearly undergoing major interactions with nearby companions (Chiaberge et al. 2015). Rest-frame UV emission, in the form of blobs most likely associated with star forming regions, is strongest in the northeastern-most part of the host galaxy. The galaxy immediately to the south of the target also shows a fainter compact UV blob. Diffuse UV emission is also present in those areas. The VLA data show a relatively weak radio core along with two strong lobes roughly $8''$ to the north and $6''$ to the south. The radio core is aligned with the optical core of the galaxy.

6.1.2. *3C 230 (z=1.487)*

This object appears as a wide, double lobed radio galaxy. The very bright object in the center of the field is a foreground star. Just east of this star, a large number of small objects are visible in the IR image within a radius of $10''$ from our target. The morphology in our optical and IR observations

appears quite similar to that shown in the emission line images of (Steinbring 2011), and is reminiscent of the biconical structure observed in the narrow line region of many Type II AGN. The size of the NLR as estimated from our images is 24kpc. The location of the core of galaxy is at the narrowest point (i.e. at the center) of the emission line region, but it is not clearly visible in our data. The radio data show a jet to the south and two lobes with compact hot spots. The radio jet is appears to be aligned with the conical structure observed in the optical and IR images.

6.1.3. *3C 255 (z=1.355)*

Our IR image shows a collection of extended sources in the vicinity of 3C 255, which appears as the largest object in the central compact group. There are two objects to the southeast (at about 1.3″ and 2″ from the target), one to the west at 2.5″, and two elongated features to the northwest. Spectroscopic data from (Giraud 1990) suggests that all of the objects in the central compact group are members of a cluster. All of these objects, except for one of the elongated galaxies, appear in the optical image as well, suggesting that active star formation is ongoing.

Radio maps indicate a relatively weak signal at the center of the host galaxy, as well as a brighter, compact radio source, possibly a hot spot, roughly 1″ to the southeast of the host galaxy.

6.1.4. *3C 257 (z=2.474)*

3C 257 is the most distant object in our sample and it is also the highest redshift object in the 3CR catalog. Its host galaxy appears in our IR image as a bright core surrounded by a tear-drop shaped region of emission which extends primarily south and east. Its morphology is clearly distorted, most likely as a result of an ongoing major merger. There is a small amount of signal in the optical image associated with the compact brighter area, which may indicate that star formation is ongoing. This supports the relatively high star formation rate of $920^{+60}_{-50} M_{\odot}$ per year calculated using SED fitting of Herschel data for 3c 257. (Podigachowski et al. 2015)

The galaxy is surrounded by about 10 other sources within a radius of $\sim 9''$ in the IR image. Most of these sources also appear in our optical image with very faint signals in their cores. The radio core is on the optical continuum core of the galaxy. In addition, the radio data show two lobes roughly 7″ to the southeast and also to the northwest of the host.

6.1.5. *3C 297 (z=1.406)*

This target appears in our data with a complex morphology suggestive of ongoing merger activity (Chiaberge et al. 2015). In the IR image, 3C 297 appears as a compact but resolved core surrounded by an area with a radius of more than 2″ of more diffuse emission. Directly north of the core by 2″, there is an arc-shaped area of emission. Approximately 1″ south of the target there is also a highly elongated source.

In the optical image, the core of 3C 297 is resolved into two distinct areas of emission, with the eastern area much more extended than the western region. There is also faint emission associated with the extended arc-shaped area north of the target, as well as relatively strong emission from the highly elongated source south of the target, suggesting an active merger.

In addition to the sources described above, the IR image also shows 2 sources, approximately 2″ to the southwest and 2.5″ to the south of the target, which have no optical counterparts.

Radio maps show strong, wide-spread signal across the field. A lobe stretching from the galaxy more than 5″ to the northwest displays emission along its entire length. Emission to the south spreads over a much wider area, with a stronger concentration of signal centered on an elongated area approximately 1″ from the galaxy. Also present in this area are two knots of emission in the optical image, although with no radio core to aid in the alignment of the radio and visible/IR data, we cannot be completely sure of the relative positions of these sources.

6.1.6. *3C 300.1 (z=1.159)*

This galaxy appears within our IR image as an extended object containing a bright nucleus within an area of diffuse stellar emission. Also present within the extended envelope is a localized region of increased brightness to the southwest of the galaxy center. This is the only region of the galaxy other than the core that also appears within our optical image, suggesting an area of active star formation. The overall morphology is irregular most likely as a result of a recent merger event. Numerous extended sources are visible in the IR image around the central galaxy. Only a handful of these also show signal in the optical image.

Radio maps show two bright, extended lobes to the north and south of the host galaxy by roughly 4″ and 2″ respectively, but no emission in the galaxy core at 8.4 GHz.

6.1.7. *3C 305.1 (z=1.132)*

This galaxy clearly appears in our IR image with a complex morphology suggestive of ongoing merger activity, and includes an extended, bright central area surrounded by more diffuse signal. Approximately 1.5″ north of the brightest emission, there is a highly elongated galaxy running almost directly east-west. In addition, there is a distinct, compact source located 2″ southwest of the center of the target.

In the optical image, the region in the center of the galaxy appears with an irregular shape spanning the same area covered by the brightest area in the IR image, suggesting wide spread star formation in the nucleus. SED-fitting of Herschel data suggests a star formation rate of $220^{+40}_{-20} M_{\odot}$ per year for 3C 305.1. (Podigachowski et al. 2015) The elongated object to the north also displays significant optical signal. The compact source to the southwest shows no significant optical signal.

The radio map shows a bright hot spot just to the north of the galactic center. There is also radio emission at the nucleus of the host galaxy. A second, weaker lobe is seen roughly 3″ south of the galactic center. The positions of the radio emission lobes is aligned with the elongation direction of the galaxy in the visible/IR data.

6.1.8. *3C 322 (z=1.168)*

This galaxy appears in our IR image as an extended object with a core that is slightly elongated in the northwest/southeast direction. There are two additional sources visible within 2.5″ of the target. In the corresponding optical image, signal from the target is limited to the northwestern-most point of the core. Only one of the two additional sources shows a limited amount of optical emission.

Corresponding radio data reveal emission within the galactic core at a location within 1″of the optical emission core. In

addition, two lobes are present directly north and south of the galaxy by roughly 10 ″ and 15 ″ respectively.

6.1.9. *3C 324 (z=1.206)*

The radio galaxy 3C 324 appears in our IR image as an extended object stretching primarily east-west, with a smooth appearance to the west, and a more irregular, blobby appearance on the eastern side. In addition, there are 3 sources within 3″ of the galactic center, including an area immediately to the west and in-line with the galaxy's semi-major axis, as well as two sources to the north and east.

The bright galactic center in the IR image has almost no signal in the corresponding optical image. The blobby appearance of the eastern half of the galaxy in the IR image is also present in the optical image, with a semi-circle of bright emission just to the east of the dark galactic center. The western half of the galaxy appears in the optical image with the brightest signal just to the west of the galactic center and a decreasing brightness to the west as the distance from the galactic center increases. This morphology is suggestive of enhanced star formation possibly associated with an ongoing merger. Using Herschel data, Podigachowski et al. (2015) calculate a star formation rate of $180^{+40}_{-30} M_{\odot}$ per year for 3C 324. In addition, the three nearby sources all show at least some signal in the optical image.

The radio map shows a compact core aligned with the bright (in the IR image) galactic center. Two extended lobes and two knotty jets are roughly aligned with the optical emission, stretching from just outside the galactic core to nearly 10″ northeast and southwest. One of the knots within the the eastern jet appears to be aligned with a source in the IR image. However, uncertainty on the position of the nucleus makes this alignment unsure. Approximately 4″ to the west of the radio core, the jet bends to the south. At nearly the same location as the bend, we see a galaxy in our IR and optical images. It is possible that this galaxy is forcing the jet to bend and causing the western lobe out of alignment with the jet.

6.1.10. *3C 326.1 (z=1.825)*

This galaxy appears in our IR image as a relatively dim, elongated source stretching primarily east-west. The target is also surrounded by many small irregularly-shaped sources, several of which are within 1″ of the galactic center and nearly overlapping with the galactic edges, suggesting possible merger activity. Outside of these closest sources, there are numerous dim sources primarily north of the target, out to about 8″ from the target.

In our optical image, the target itself shows no significant emission. Of the small surrounding sources, several show a small amount of signal, including one of the sources closest to the target.

The corresponding radio map shows two compact lobes east and west of the galaxy by 3 ″. The lobe to the west shows significantly stronger emission than the lobe to the east. The lobes are roughly colinear with the elongation direction of the galaxy in the IR image. The signal in the IR image is most likely contaminated by [OIII] emission line flux.

6.1.11. *3C 356 (z=1.079)*

The radio source 3C 356 appears in our IR image associated with two main bright elliptical galaxies lying on a southeast-northwest line, separated by 5″. The northern source appears brighter and more compact than the southern source. There are also 5-6 smaller distinct sources between the two main sources.

In contrast, our optical image shows emission in the form of a bi-conical structure from the northern of the two main sources. There is also faint signal in the optical image associated with two of the more extended surrounding objects, as well as the compact object located between and equidistant from the two main sources.

This is clearly a merging system, with active star formation occurring in at least some of the sources connecting the two main galaxies (Chiaberge et al. 2015).

The corresponding radio map shows two compact radio sources aligned with both of the bright IR components. In addition there are two lobes, roughly 30 ″ to the north and 15 ″ to the south of the bright IR components. The lobes are well aligned with the two main IR image sources. The northern source is the host of the FR II radio galaxy. (Cimatti et al. 1997)

6.1.12. *3C 454.1 (z=1.841)*

3C 454.1, a Compact Steep Spectrum (CSS) source (e.g O'Dea (1998)) showing signs of recent merger activity (Chiaberge et al. 2015), appears in our IR image as a double-lobed object oriented north-south. The northern lobe is significantly brighter than the southern lobe. In addition, there are 4 distinct objects within about 3.5″ of the target. The optical image shows essentially no emission from any of these objects, despite a calculated star formation rate of $750^{+40}_{-70} M_{\odot}$ per year (Podigachowski et al. 2015). This may imply that dust obscuration in this object is substantial.

The radio maps associated with the target show compact radio sources that are well aligned with the bright cores in the IR image.

6.2. *QSOs*

6.2.1. *3C 68.1 (z=1.238)*

This QSO appears in our IR image as a bright compact object. There are only two other sources within 8″ of the target. These are both smaller, dimmer sources 3.75″ and 5.5″ to the east. Neither of these extra sources is visible in the corresponding optical image. The radio map of the area shows emission in the core of the quasar, as well as two lobes roughly 10″ to the north and 15 ″ to the south.

Our photometry show that 3C 68.1 is significantly redder than all of our other QSO targets. This is most likely due a combination of a high inclination and a dusty environment. This allows dust-reddened light from the nucleus as well as reddened scattered light to contribute to the overall observed signal. (Brotherton et al. 1998)

6.2.2. *3C 186 (z=1.069)*

The target, a well-studied CSS source (O'Dea 1998) appears in our IR image in an overdense region which is most likely a cluster of galaxies (Siemiginowska et al. 2008). The host galaxy is clearly visible as a roughly elliptical area of diffuse emission extending to the northeast and southwest.

A blob of relatively bright emission, about 1″ in size, has its center located roughly 2″ northeast of the target. Our optical image reveals a well-defined area of signal in the same area, suggesting active star formation. Very few of the galaxies surrounding the target have appreciable signal in the optical image, supporting the assertion that they are cluster members at the redshift of the QSO.

Radio data show emission coincident with the core of the QSO, as well as a jet extending from the QSO to the northwest for roughly 2″. The signal in this jet is concentrated in two distinct knots. There is also an area of emission visible to the southeast of the QSO core.

6.2.3. *3C 208 (z=1.112)*

In our IR image, 3C 208 appears as a compact object in our data, with 25-30 sources visible within 15″. The closest source is just over 1″ northeast of the target. Most of these surrounding objects show a limited amount of signal in our optical image. There is corresponding radio emission coming from the core of the QSO, as well as lobes stretching roughly 6″ east and west.

6.2.4. *3C 220.2 (z=1.157)*

3C 220.2 appears in our IR and optical images as a compact source with a few immediate neighbors, located within a group of large spiral galaxies. In the IR there are 5 sources to the south and one to the northwest, all within 6″. There is little to no signal from these sources in our optical image.

Radio data show signal centered on the QSO, as well as two lobes to the northeast and southwest. There is evidence of a hot spot in the southwestern lobe. The peak of the radio signal in the hot spot is coincident with an area visible in our optical image.

6.2.5. *3C 268.4 (z=1.402)*

Our IR image of 3C 268.4 reveals a bright QSO with a handful of small, dim sources, within about 12″. In addition, the nearest neighbor to the target is a relatively bright, compact object roughly 2.5″ to the south. In our optical image, this nearest neighbor is resolved into a clumpy mass with significant signal, suggesting active star formation.

Many of the other nearby dim sources also exhibit some flux in the optical. Finally, the optical image also contains an oblong source located only 0.8″ to the southwest of the target, suggesting a possible merger. If there is corresponding flux from this object in our IR image, it is not visible due to its close proximity to the target and the large pixel size in the IR channel.

Radio emission is also visible coming from this adjacent oblong source. The QSO itself shows significant signal in the radio. There are also two radio lobes, roughly 3″ to the northeast and southwest.

6.2.6. *3C 270.1 (z=1.528)*

3C 270.1 appears as a bright unresolved source surrounded by many dimmer sources of various morphologies. There are at least 5 sources within 4″ of the target. Of these, only one is detected in our optical image. Most of the sources in the region surrounding the object are very red.

The radio morphology is not symmetric with respect to the center of the QSO. In addition to radio signal present at the core of the QSO itself, we see radio lobes to the south and the northwest. Also visible is a jet connecting the radio core and the southern lobe. No jet is visible on the northern side of the core. The radio morphology is reminiscent of that of wide angle tailed (WAT) sources (Gómez et al. 1997), which typically inhabit clusters of galaxies.

6.2.7. *3C 287 (z=1.055)*

Our IR image of 3C 287 reveals the bright QSO with bright compact neighbor 4″ to the southwest. In addition, four sources of varying brightnesses are present along a line separating the target from the bright neighboring source. Of these 4 sources, 2 show some signal in our optical image. The associated radio signal is limited to a compact core on the optical core of the QSO.

6.2.8. *3C 298 (z=1.438)*

In our IR image, 3C 298 appears as a bright, asymmetrical source with more signal to the east appearing in a conical shape reminiscent of the narrow line region seen in 3C 230.

In addition, there is a small area of increased flux 2.5″ to the southeast of the galaxy center in our IR image. This area is elongated and points radially away from the center of the QSO. In the optical image, with its better resolution, this small source appears as three knots of emission. These sources could be regions of intense star formation at the edge of the NLR.

Radio emission is visible in the core of the QSO, as well as two small areas 0.5″ and 1.5″ to the east; probably a knotty jet and a hot spot. The jet and hot spot appear roughly in the center of the conical area of emission in the IR and optical images. Note that the jet is at a different orientation than the three knots of optical emission to the southeast of the QSO.

6.2.9. *3C 418 (z=1.686)*

The QSO 3C 418 appears in our IR image as a bright target located within a dense field of objects. In addition to the main QSO, there appears to be a distinct source located 1.5″ to the southwest, as well as a small and a larger extended source 3″ and 6″ to the northwest, respectively. To the east, there is also a pair of extended sources approximately 8″ from the target. While 3C 418 appears in our optical image as a compact source, only the source 3″ to the northwest shows any signal in the optical image.

Radio emission is concentrated in the core of the QSO, with a small jet extending approximately 6″ to the northwest.

6.2.10. *3C 432 (z=1.785)*

3C 432 appears in our IR data as an unresolved source within a field of objects. There is some dim extended emission, potentially a narrow line region, to the northwest of the QSO. There are also several distinct sources in the same direction as the extended emission, within 7.5″ of the QSO. In addition a small source is located 2″ to the northeast, and two extended sources are 4.9″ to the south of the target.

In our optical image, 3C 432 appears as a compact, isolated source. None of the nearby sources described above show optical signal.

Radio emission is present in the core of the QSO, as well as in two lobes roughly 6-8″ to the northwest and southeast. These lobes are aligned with the potential NLR-emission seen in our IR image.

7. CONCLUDING REMARKS

We have presented qualitative descriptions along with photometric analyses of new WFC3 visible and near-IR observations of a set of 22 $1 > z > 2.5$ radio galaxies and QSOs from the 3CR catalog. In addition, archival radio data have been combined with the HST observations in order to provide a more complete picture of the targets and their local environments.

Our photometric analysis has shown that RGs are generally more red than the QSOs. We also find that for QSOs, increasing IR channel flux is correlated with increased redness.

Emission line analysis indicates that the contamination from emission line signal is limited for both the QSOs and the radio galaxies. We find contamination rates of less than 2.6% from each of the lines for which we have direct flux measurements. However, we do not estimate contributions from the potentially bright Hα and [OIII] lines in the rest frame optical data.

For most of our radio galaxies, we see the alignment effect, where the lobes in the radio data are colinear with the major axis of the galaxy in the visible/IR image. However, emission line contamination means that for most sources, we are unable to distinguish between alignment with the optical continuum versus alignment with the emission line gas.

We see two RGs (3C 322 and 3C 356) with compact nuclei coincident (to within WCS uncertainties) with the radio core. Extended narrow line regions appear visible in 2 RGs (3C 230 and 3C 305.1) and 5 QSOs (3C 186, 3C 268.4, 3C 270.1, 3C 298, and 3C 432). In addition we observe clumps of UV emission, most likely regions of active star formation, in 4 of the RGs (3C 210, 3C 305.1, 3C 324, and 3C 326) and two of the QSOs (3C 186 and 3C 268.4). One of our sources, 3C 356, appears to be a double AGN. Finally, 3 RGs (3C 230, 3C 255, and 3C 305.1) and 2 QSOs (3C 220.2 and 3C 298) show evidence of hot spots in their radio maps.

The authors would like to thank the referee for a careful reading of our manuscript and many helpful comments, which enabled us to greatly improve the final document. J.P.K. and B.H. acknowledge support from *HST*-GO-13023.005-A. This research has made use of the NASA/IPAC Extragalactic Database (NED) which is operated by the Jet Propulsion Laboratory, California Institute of Technology, under contract with the National Aeronautics and Space Administration. This work is based on observations made with the NASA/ESA HST, obtained from the Data Archive at the Space Telescope Science Institute, which is operated by the Association of Universities for Research in Astronomy, Inc., under NASA contract NAS 5-26555. This work is based in part on observations taken by the VLA, operated by U.S. National Radio Astronomy Observatory which is a facility of the National Science Foundation, operated under cooperative agreement by Associated Universities, Inc.

Facilities: HST (WFC3), VLA

REFERENCES

Ahn, C. P., Alexandroff, R., Allende Prieto, C., et al. 2012, ApJS, 203, 21
Anderson, J. & Bedin L., 2010, PASP, 122, 895, 1035
Baars, J. W. M., Genzel, R., Pauliny-Toth, I. I. K., 1977, A&A61, 99
Baum, S. A., & Heckman, T. 1989, ApJ, 336, 681
Bennett, A. S., 1962, MNRAS, 68, 163
Bennett, A. S., 1962, MNRAS, 125, 75
Bertin, E. & Arnouts, S., 1996, A&AS, 317, 393
Blandford, R. D., Netzer, H., Woltjer, L., 1990, Active Galactic Nuclei (New York: Springer-Verlang)
Brotherton, M. S., Wills, Beverley J., Dey, A. et al. 1998, ApJ501, 110
Chiaberge, M., Gilli, R., Lotz, J. M., & Norman, C. 2015, ApJ, 806, 147
Cimatti,A., Dey, A., van Breugel, W. et al. 1997, ApJ476, 684
Deustua, S., WFC3 Data Handbook, Version 4.0 (Baltimore: STScI)
Dressel, L. 2014, Wide Field Camera 3 Instrument Handbook, Version 6.0 (Baltimore: STScI)
Eales, S. & Rawlings, S., 1996, ApJ, 460, 68
Eisenstein, D. J., Weinberg, D. H., Agol, E., et al. 2011, AJ, 142, 72
Giraud, E., 1990, A&A, 234, 20
Gómez, P. L., Pinkney, J., Burns, J. O., et al. 1997, ApJ, 474, 580
Gonzaga, S., Hack, W., Fruchter, A., Mack, J., eds., 2012, The DrizzlePac Handbook. (Baltimore, STScI)
Grimes, Rawlings, S. & Willott, 2004, MNRAS, 349, 503
Jackson, N. & Rawlings, S., 1997, MNRAS, 286, 241
Kellermann, K. I., Pauliny-Toth, I. I. K., Williams, P. J. S., 1969, ApJ, 157, 1
Lacy, M., & Rawlings, S. 1994, MNRAS, 270, 431
Madrid, J. P., Chiaberge, M., Floyd, D., et al. 2006, ApJS, 164, 307
Miley, G. and De Breuck, C., 2008, A&A Rev., 15, 67
Netzer, H. 1990, Active Galactic Nuclei, 57
Long, K., Wheeler, T., Bushouse, H., 2011, WFC3 Instrument Science Report 2011-09 (Baltimore, STScI)
Podigachowski, P., Barthel, P. D., Haas, M. et al. 2015, A&A, 575, A80
Polletta, M., Tajer, M., Maraschi, L. et al. 2007, ApJ, 663, 81
O'Dea, C. 1998, PASP, 110, 493
Sekhon, Jasjeet S., 2011, Journal of Statistical Software 42, 1
Siemiginowska, A., LaMassa, S., Aldcroft, T. L., Bechtold, J., & Elvis, M. 2008, ApJ, 684, 811-821
Spinrad, H., Marr, J., Aguilar, L., Djorgovski, S., PASP, 97, 932
Stanford, S. A., Eisenhardt, P. R., Dickinson, M., Holden, B. P., & De Propris, R. 2002, ApJS, 142, 153
Steinbring, E., 2011, AJ, 142, 172
Tremblay, G. R., Chiaberge, M., Sparks, W. B., et al. 2009, ApJS, 183, 278
Vanden Berk, D. E., Richards, G. T., Bauer, A. et al., 2001, AJ, 122, 549
van Dokkum, P., 2001, PASP, 113, 1420
Wilkes, B. J., Kuraszkiewicz, J., Haas, M. et al., 2013, ApJ, 773, 15
Willot, C. J., Rawlings, S., Blundell, K. M., 1999, MNRAS, 309, 1017
Workman, B., Jordan, I. Chapman, G. et al., 2014, *HST User Information Report UIR-2014-001.*

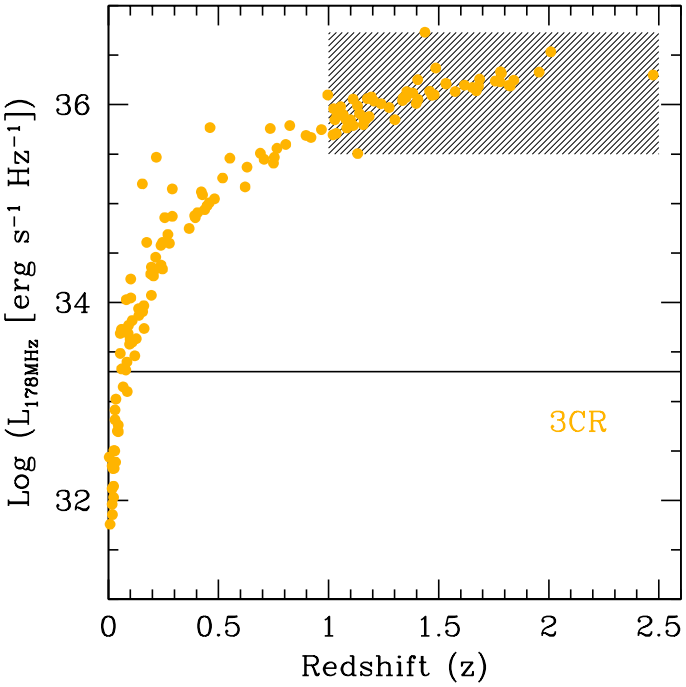

FIG. 1.— The distribution in radio power (at 178MHz) and redshift of the entire 3CR catalog. The shaded area corresponds to the sample of our HST SNAPSHOT program described in this paper.

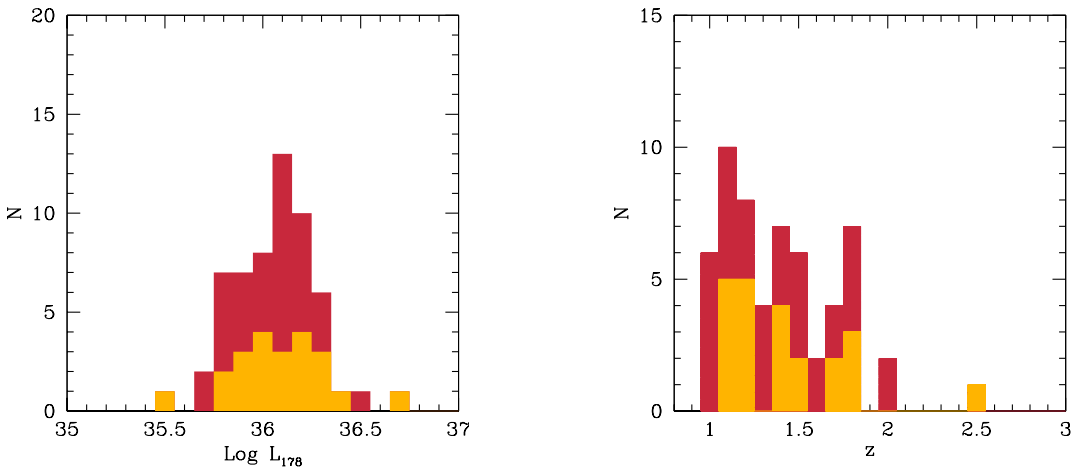

FIG. 2.— The distribution in total radio power per unit frequency (at 178MHz, left panel) and redshift (right panel) for the whole 3CR sample with $z > 1$ (in red) and for the observed sub-sample (yellow).

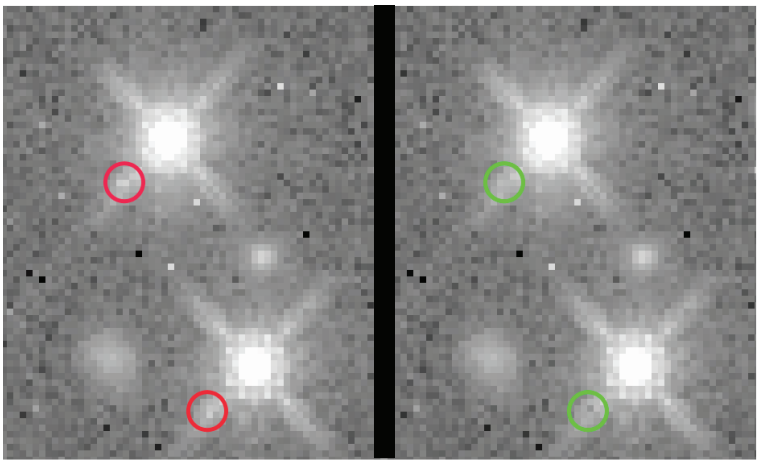

FIG. 3.— Example of self-persistence, seen in before and after versions of our second image of 3C 287. On the left side, persistence signal is visible inside the red circles. This persistence is from the cores of these same objects in our first 3C 287 image. The persistence is offset from the cores in the second image due to our 1.25″ dither between images. On the right, we show the persistence-cleaned version of the image. Note that in the green circles, the persistence is no longer visible.

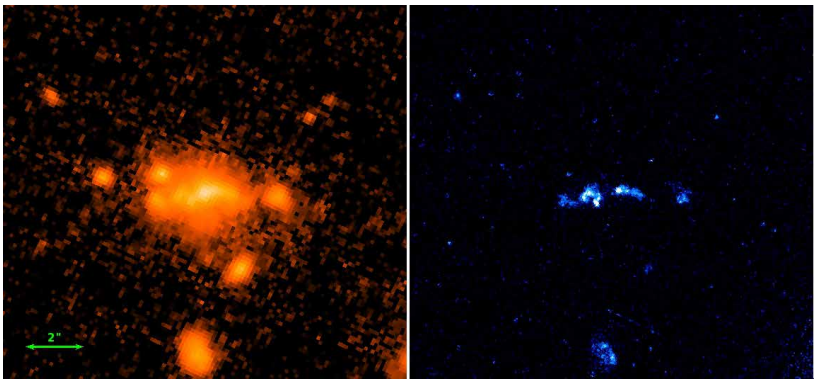

FIG. 4.— 3C 324 IR and UVIS images. We use the photometric apertures defined in the IR image for photometry in the UVIS data to avoid counting each small star forming region as a separate source.

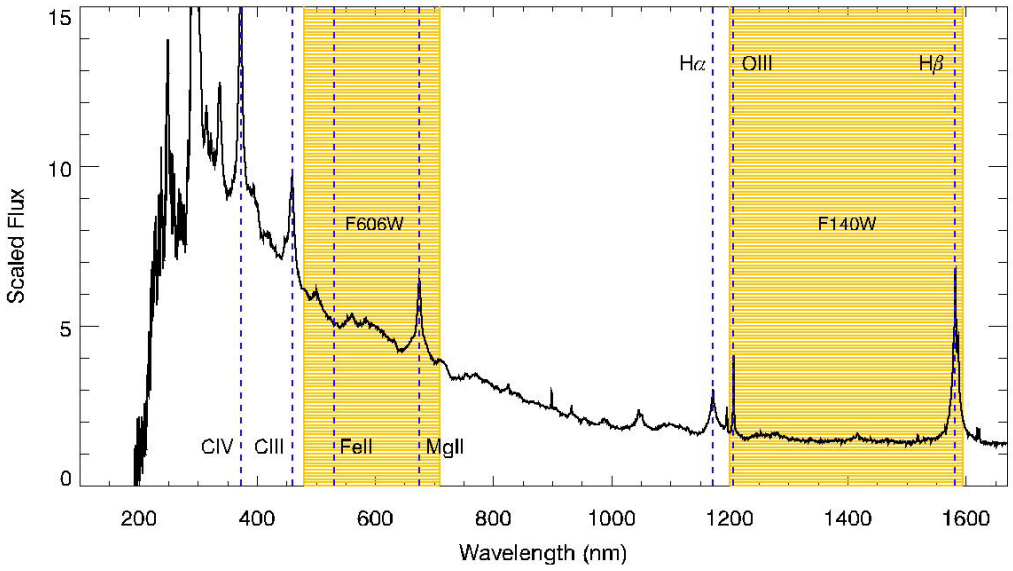

FIG. 5.— This figure shows an example QSO spectrum (from Vanden Berk (2001)) redshifted to z=1.41 (roughly matching 3C 268.4), plotted on top of the bandpasses for the F606W (left) and F140W (right) filters, shown in yellow. In this case, two emission lines are present within each of the filter bandpasses.

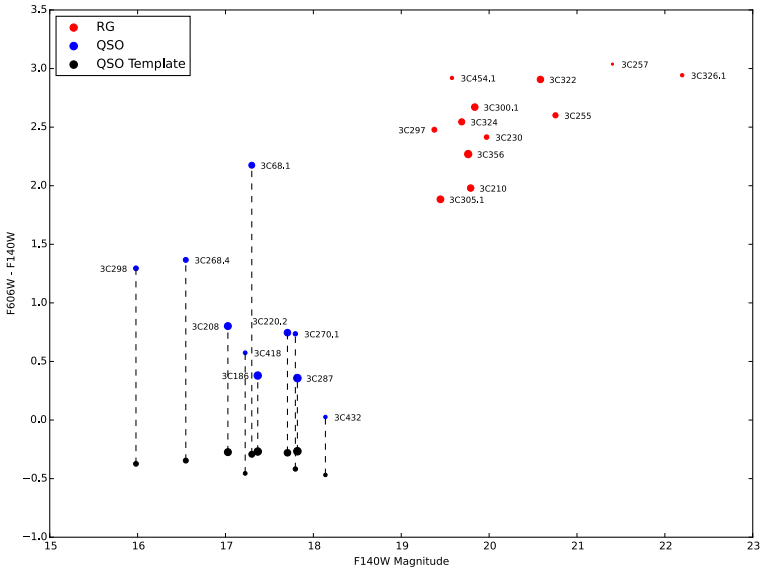

FIG. 6.— CMD for all of our targets. Red points show results for the radio galaxies, and blue points represent QSOs. The size of the data points is inversely proportional to the targets' redshift values. This shows that two of our farthest targets (3C 257 and 3C 326.1) are also the reddest. The black points show calculated colors from a template QSO spectrum that has been redshifted and renormalized to match the F140W magnitudes of each of our targets.

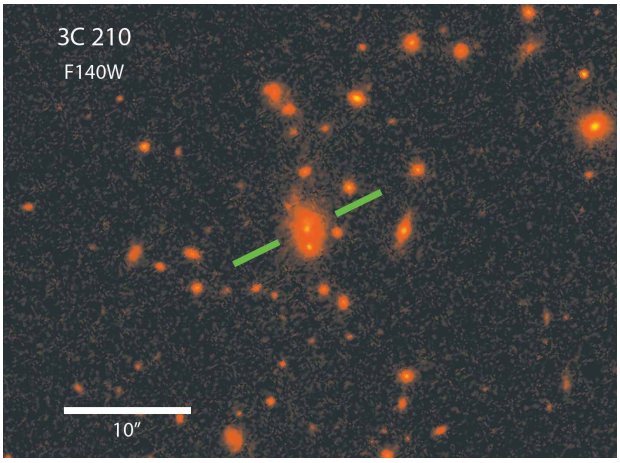

FIG. 7.— Central $35'' \times 50''$ of the IR image of RG 3C 210. The image has been rotated so that North is up and East to the left. Green lines are placed on either side of the target to help identify its location.

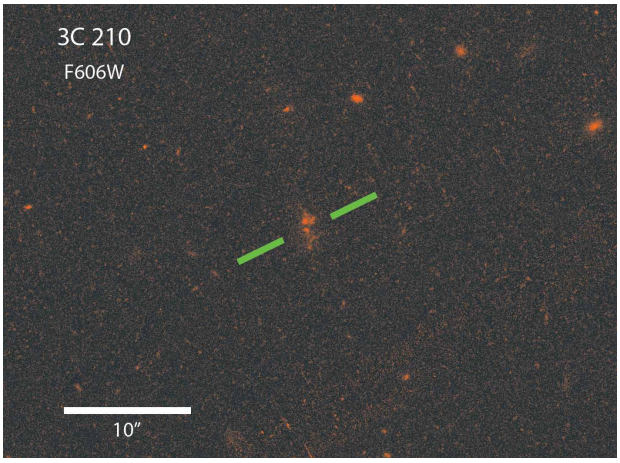

FIG. 8.— Central $35'' \times 50''$ of the UVIS image of RG 3C 210. The image has been rotated so that North is up and East to the left. Green lines are placed on either side of the target to help identify its location.

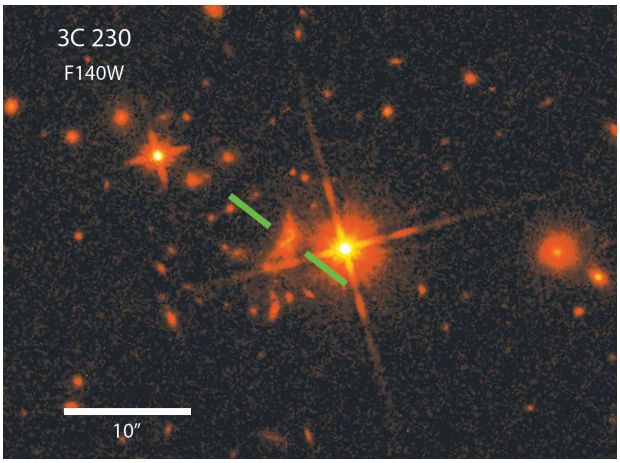

FIG. 9.— Central 35″ × 50″ of the IR image of RG 230. The image has been rotated so that North is up and East to the left. Green lines are placed on either side of the target to help identify its location.

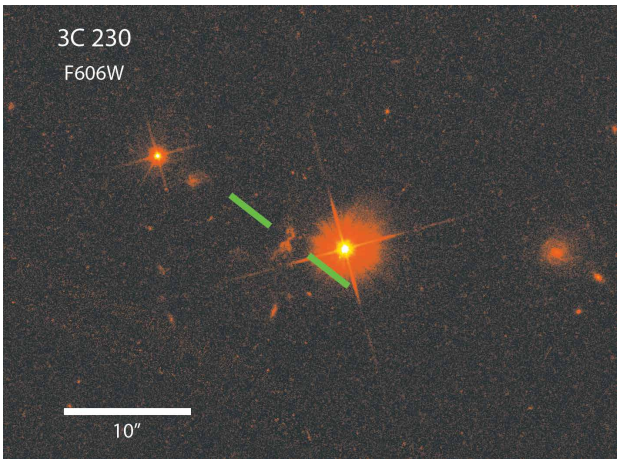

FIG. 10.— Central 35″ × 50″ of the IR image of RG 3C 230. The image has been rotated so that North is up and East to the left. Green lines are placed on either side of the target to help identify its location.

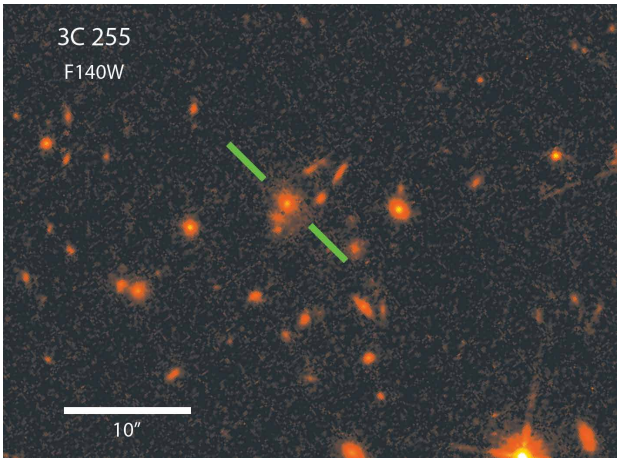

FIG. 11.— Central 35″ × 50″ of the IR image of RG 3C 255. The image has been rotated so that North is up and East to the left. Green lines are placed on either side of the target to help identify its location.

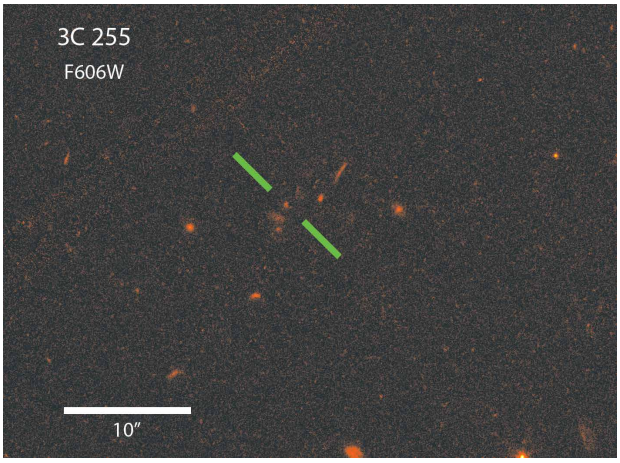

FIG. 12.— Central 35″ × 50″ of the UVIS image of RG 3C 255. The image has been rotated so that North is up and East to the left. Green lines are placed on either side of the target to help identify its location.

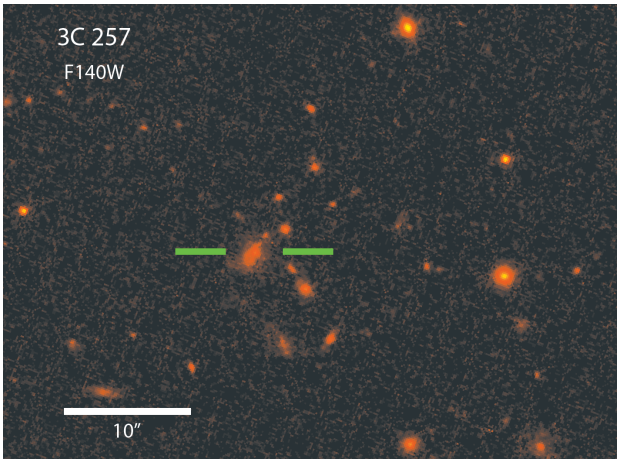

FIG. 13.— Central 35″ × 50″ of the IR image of RG 3C 257. The image has been rotated so that North is up and East to the left. Green lines are placed on either side of the target to help identify its location.

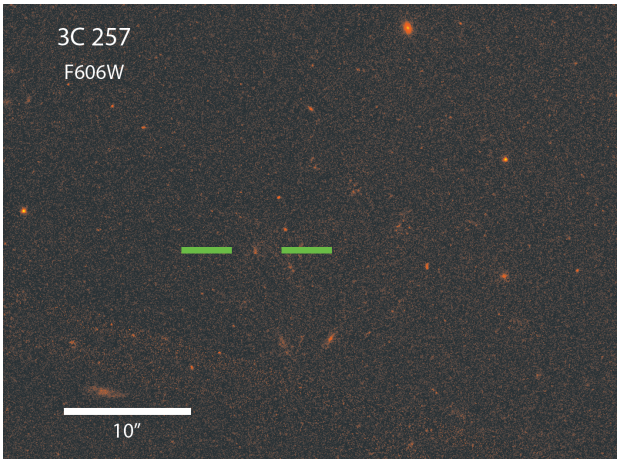

FIG. 14.— Central 35″ × 50″ of the UVIS image of RG 3C 257. The image has been rotated so that North is up and East to the left. Green lines are placed on either side of the target to help identify its location.

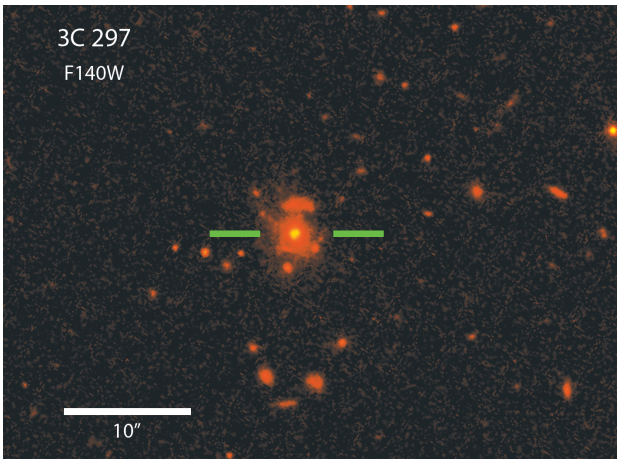

FIG. 15.— Central 35″ × 50″ of the IR image of RG 3C 297. The image has been rotated so that North is up and East to the left. Green lines are placed on either side of the target to help identify its location.

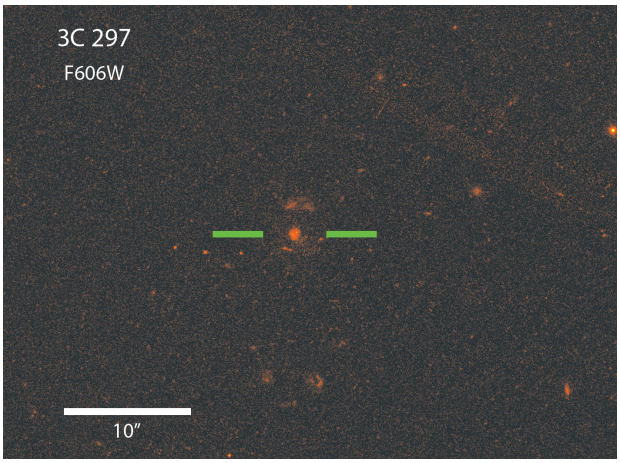

FIG. 16.— Central 35″ × 50″ of the UVIS image of RG 3C 297. The image has been rotated so that North is up and East to the left. Green lines are placed on either side of the target to help identify its location.

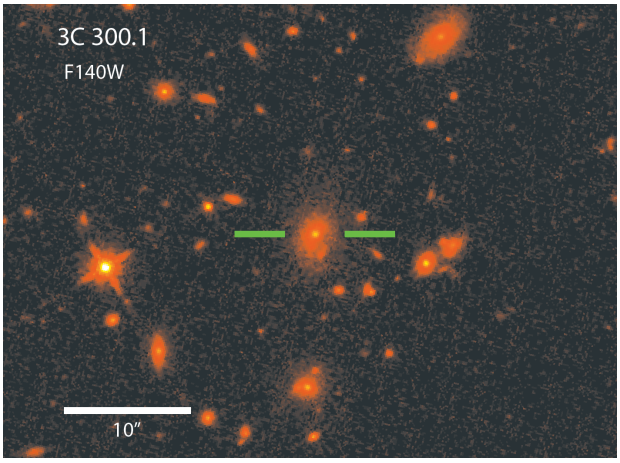

FIG. 17.— Central 35″ × 50″ of the IR image of RG 3C 300.1. The image has been rotated so that North is up and East to the left. Green lines are placed on either side of the target to help identify its location.

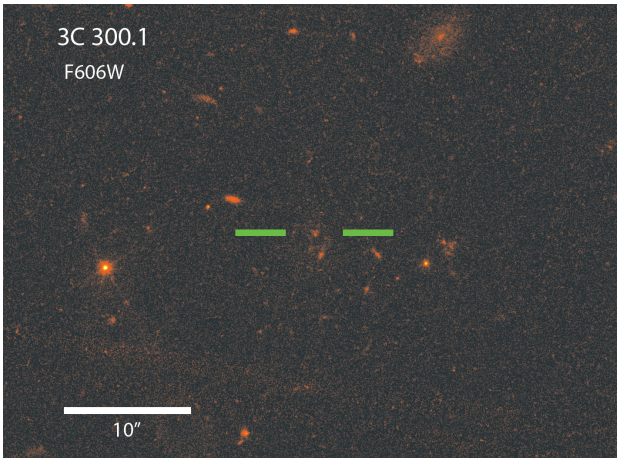

FIG. 18.— Central 35″ × 50″ of the UVIS image of RG 3C 300.1. The image has been rotated so that North is up and East to the left. Green lines are placed on either side of the target to help identify its location.

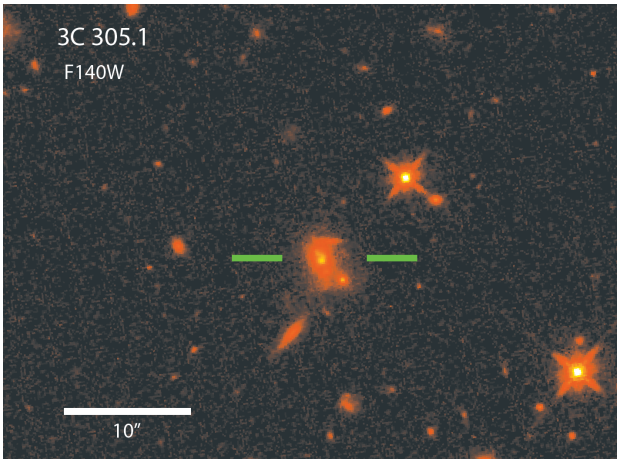

FIG. 19.— Central 35″ × 50″ of the IR image of RG 3C 305.1. The image has been rotated so that North is up and East to the left. Green lines are placed on either side of the target to help identify its location.

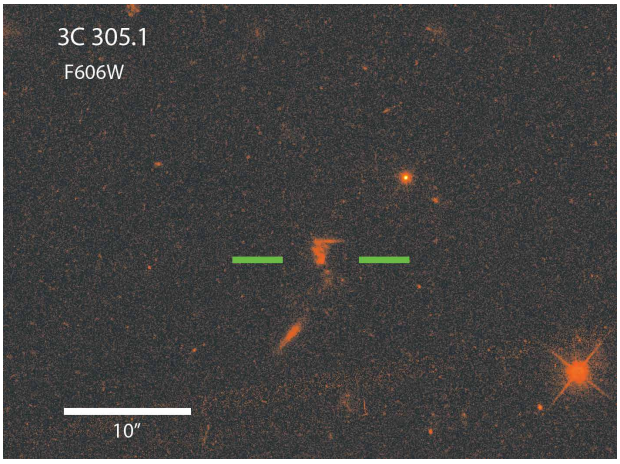

FIG. 20.— Central 35″ × 50″ of the UVIS image of RG 3C 305.1. The image has been rotated so that North is up and East to the left. Green lines are placed on either side of the target to help identify its location.

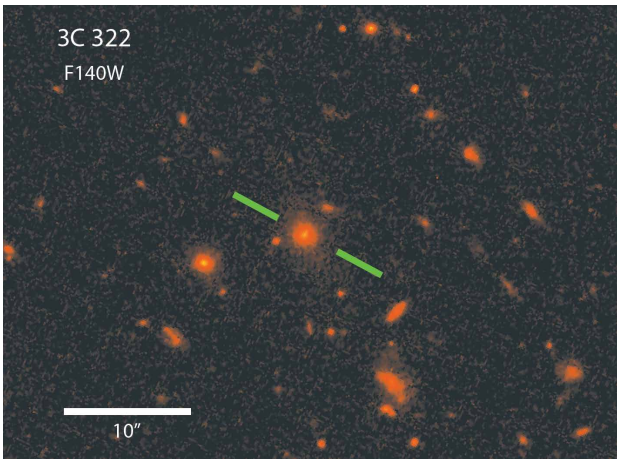

FIG. 21.— Central 35″ × 50″ of the IR image of RG 3C 322. The image has been rotated so that North is up and East to the left. Green lines are placed on either side of the target to help identify its location.

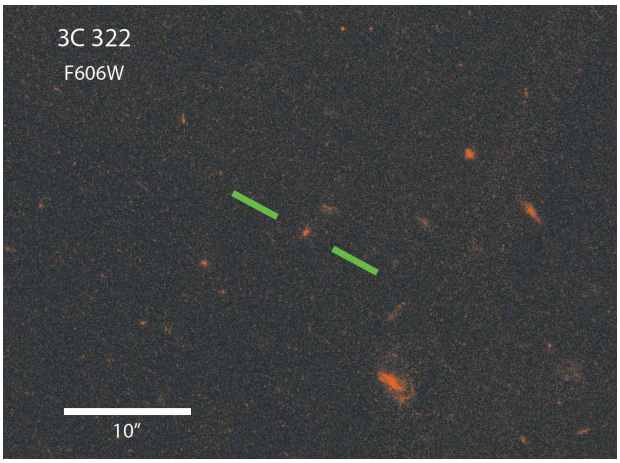

FIG. 22.— Central 35″ × 50″ of the UVIS image of RG 3C 322. The image has been rotated so that North is up and East to the left. Green lines are placed on either side of the target to help identify its location.

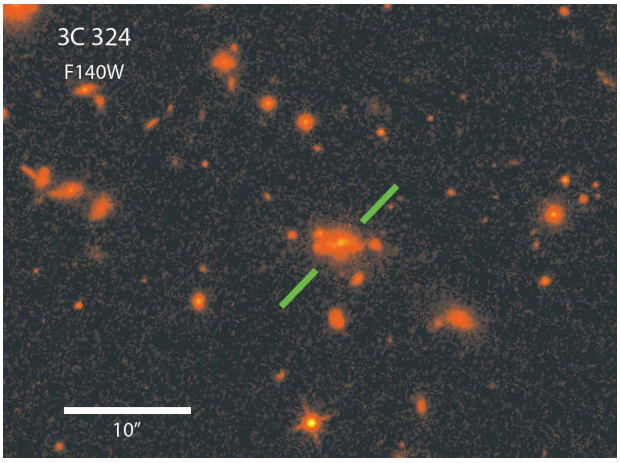

FIG. 23.— Central 35″ × 50″ of the IR image of RG 3C 324. The image has been rotated so that North is up and East to the left. Green lines are placed on either side of the target to help identify its location.

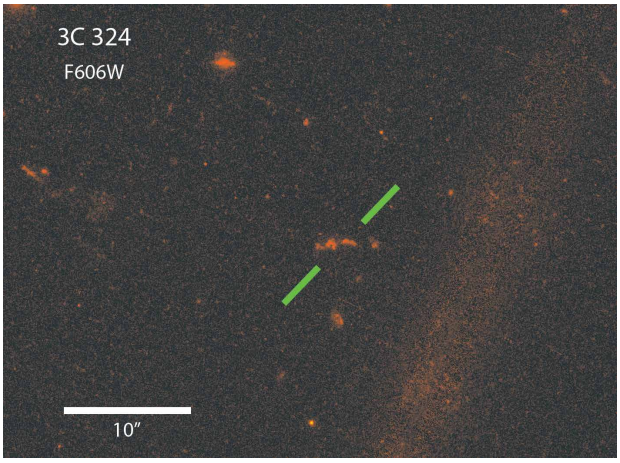

FIG. 24.— Central 35″ × 50″ of the UVIS image of RG 3C 324. The image has been rotated so that North is up and East to the left. Green lines are placed on either side of the target to help identify its location.

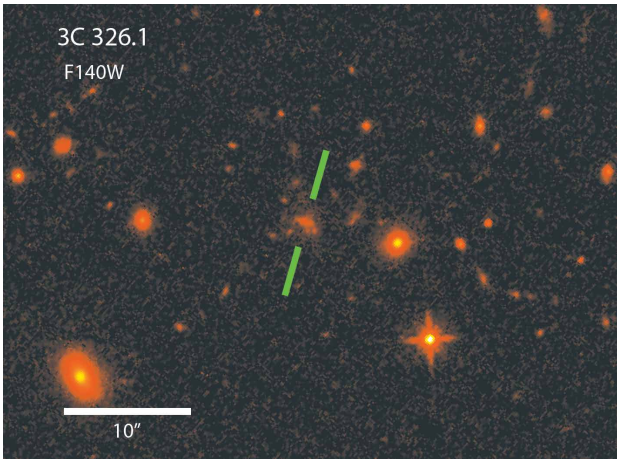

FIG. 25.— Central 35″ × 50″ of the IR image of RG 3C 326.1. The image has been rotated so that North is up and East to the left. Green lines are placed on either side of the target to help identify its location.

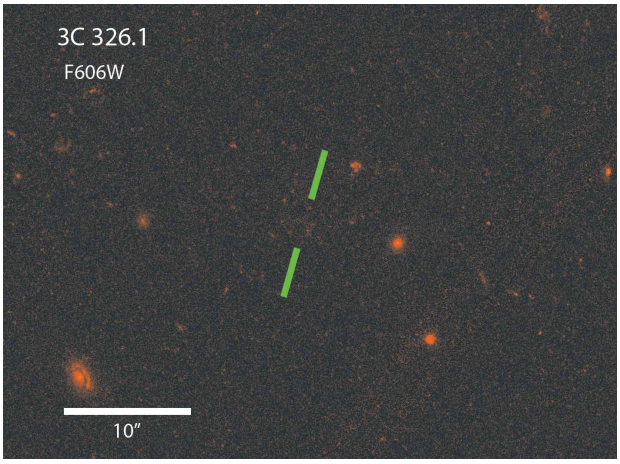

FIG. 26.— Central 35″ × 50″ of the UVIS image of RG 3C 326.1. The image has been rotated so that North is up and East to the left. Green lines are placed on either side of the target to help identify its location.

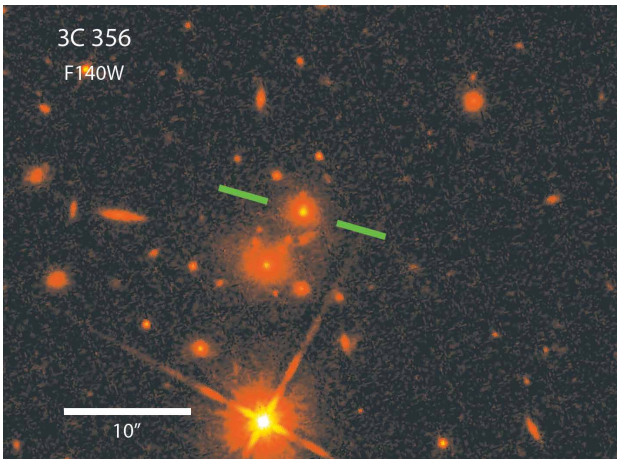

FIG. 27.— Central 35″ × 50″ of the IR image of RG 3C 356. The image has been rotated so that North is up and East to the left. Green lines are placed on either side of the target to help identify its location.

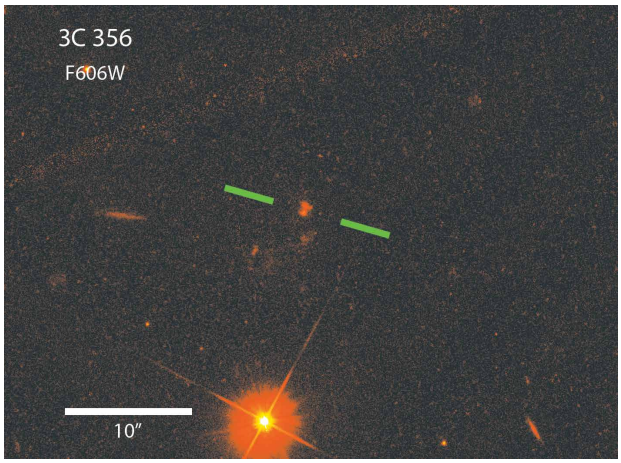

FIG. 28.— Central 35″ × 50″ of the UVIS image of RG 3C 356. The image has been rotated so that North is up and East to the left. Green lines are placed on either side of the target to help identify its location.

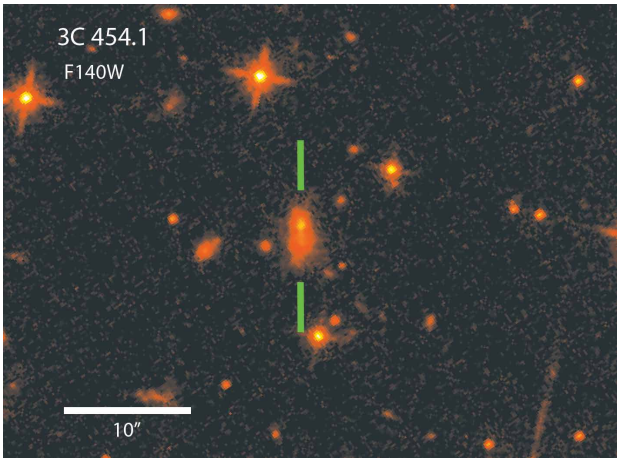

FIG. 29.— Central 35″ × 50″ of the IR image of RG 3C 454.1. The image has been rotated so that North is up and East to the left. Green lines are placed on either side of the target to help identify its location.

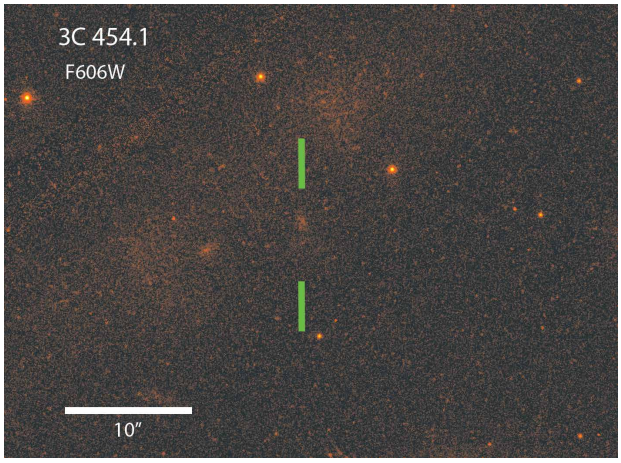

FIG. 30.— Central 35″ × 50″ of the UVIS image of RG 3C 454.1. The image has been rotated so that North is up and East to the left. Green lines are placed on either side of the target to help identify its location.

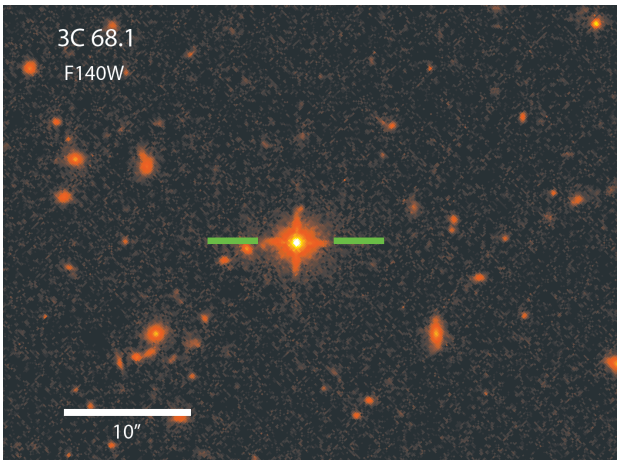

FIG. 31.— Central 35″ × 50″ of the IR image of QSO 3C 68.1. The image has been rotated so that North is up and East to the left. Green lines are placed on either side of the target to help identify its location.

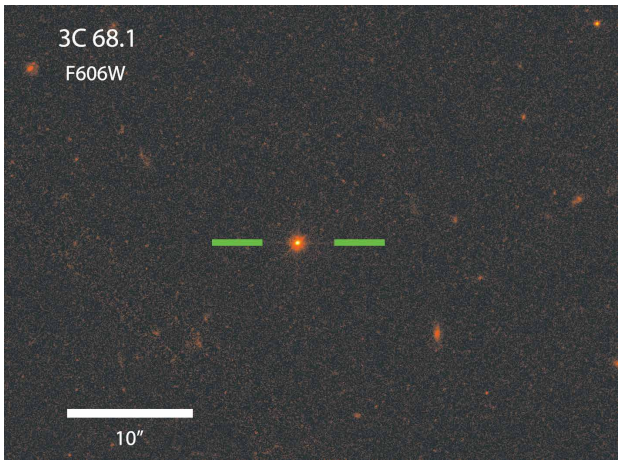

FIG. 32.— Central 35″ × 50″ of the UVIS image of QSO 3C 68.1. The image has been rotated so that North is up and East to the left. Green lines are placed on either side of the target to help identify its location.

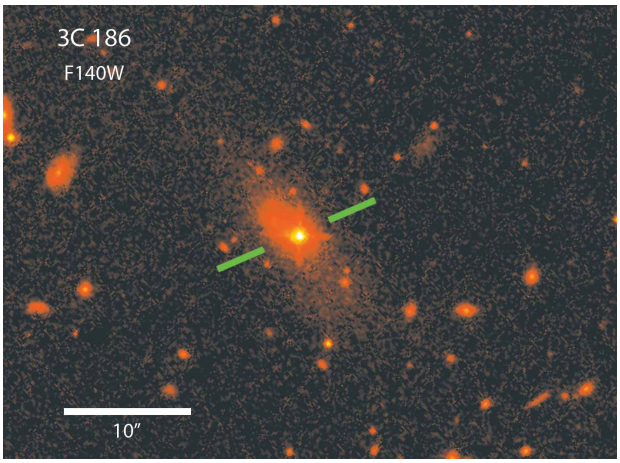

FIG. 33.— Central 35″ × 50″ of the IR image of QSO 3C 186. The image has been rotated so that North is up and East to the left. Green lines are placed on either side of the target to help identify its location.

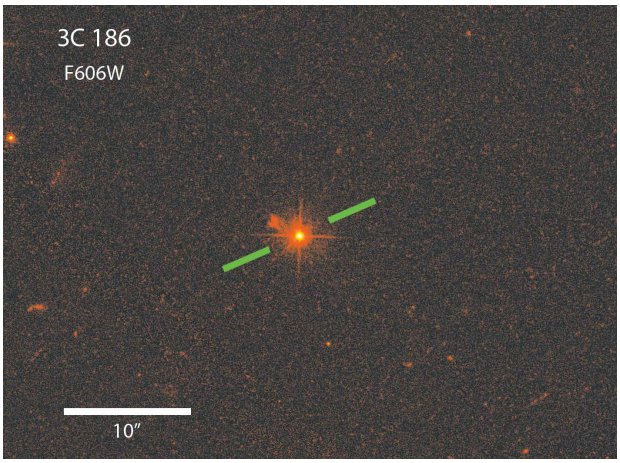

FIG. 34.— Central 35″ × 50″ of the UVIS image of QSO 3C 186. The image has been rotated so that North is up and East to the left. Green lines are placed on either side of the target to help identify its location.

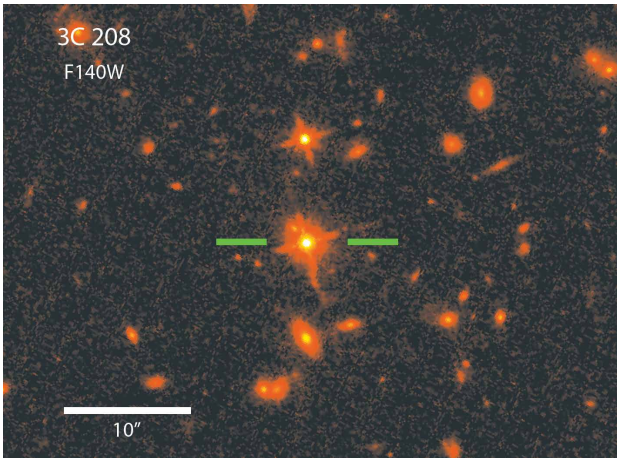

FIG. 35.— Central 35″ × 50″ of the IR image of QSO 3C 208. The image has been rotated so that North is up and East to the left. Green lines are placed on either side of the target to help identify its location.

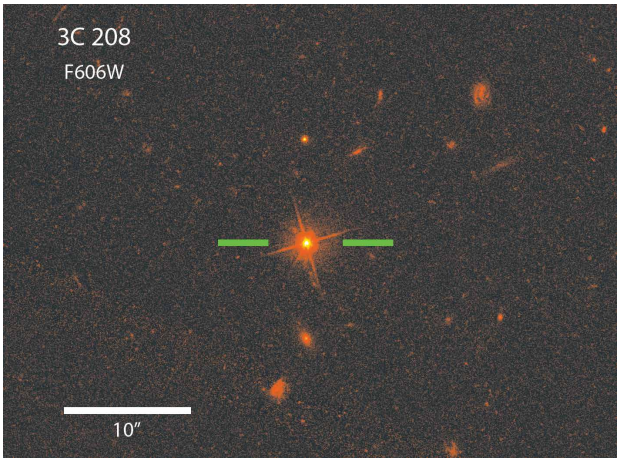

FIG. 36.— Central 35″ × 50″ of the UVIS image of QSO 3C 208. The image has been rotated so that North is up and East to the left. Green lines are placed on either side of the target to help identify its location.

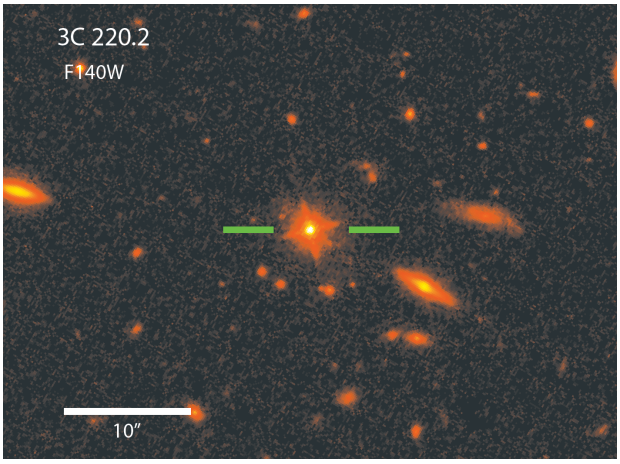

FIG. 37.— Central 35″ × 50″ of the IR image of QSO 3C 220.2. The image has been rotated so that North is up and East to the left. Green lines are placed on either side of the target to help identify its location.

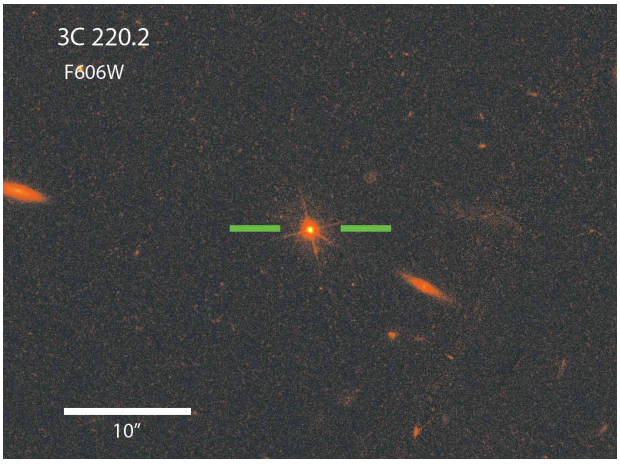

FIG. 38.— Central 35″ × 50″ of the UVIS image of QSO 3C 220.2. The image has been rotated so that North is up and East to the left. Green lines are placed on either side of the target to help identify its location.

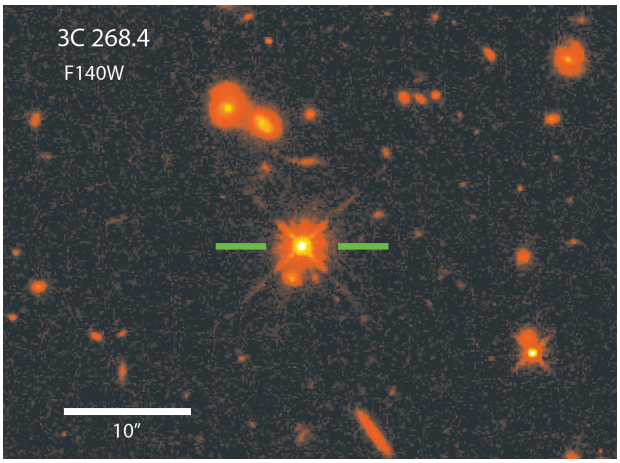

FIG. 39.— Central 35″ × 50″ of the IR image of QSO 3C 268.4. The image has been rotated so that North is up and East to the left. Green lines are placed on either side of the target to help identify its location.

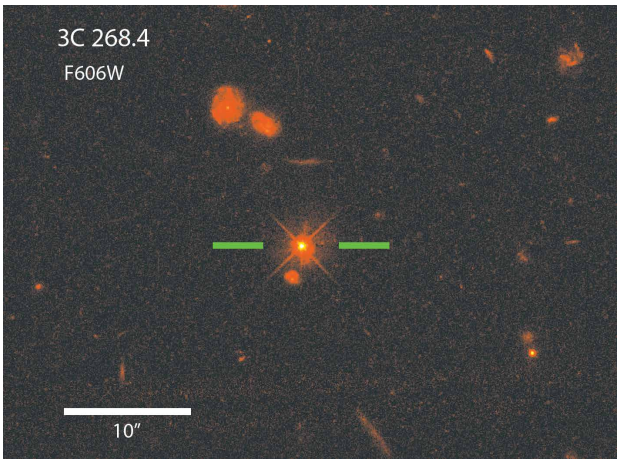

FIG. 40.— Central 35″ × 50″ of the UVIS image of QSO 3C 268.4. The image has been rotated so that North is up and East to the left. Green lines are placed on either side of the target to help identify its location.

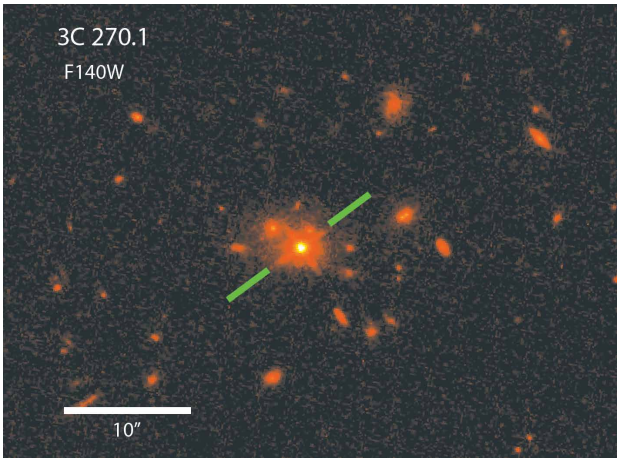

FIG. 41.— Central 35″ × 50″ of the IR image of QSO 3C 270.1. The image has been rotated so that North is up and East to the left. Green lines are placed on either side of the target to help identify its location.

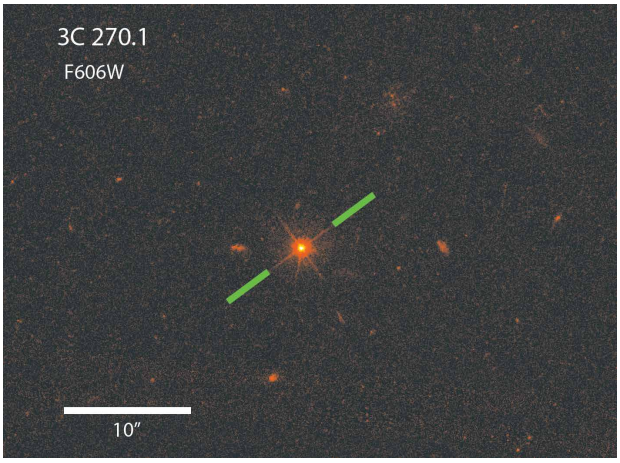

FIG. 42.— Central 35″ × 50″ of the UVIS image of QSO 3C 270.1. The image has been rotated so that North is up and East to the left. Green lines are placed on either side of the target to help identify its location.

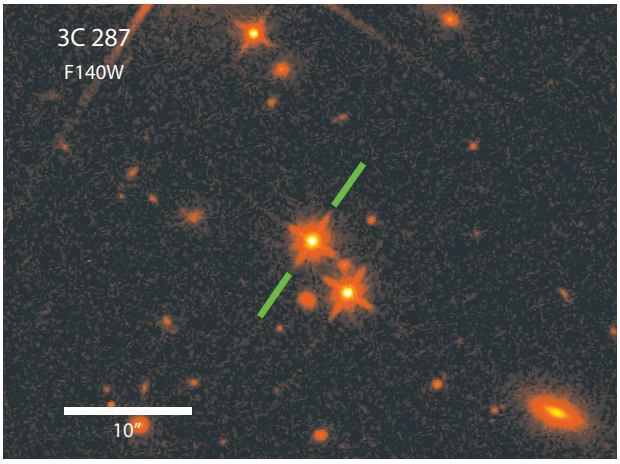

FIG. 43.— Central 35″ × 50″ of the IR image of QSO 3C 287. The image has been rotated so that North is up and East to the left. Green lines are placed on either side of the target to help identify its location.

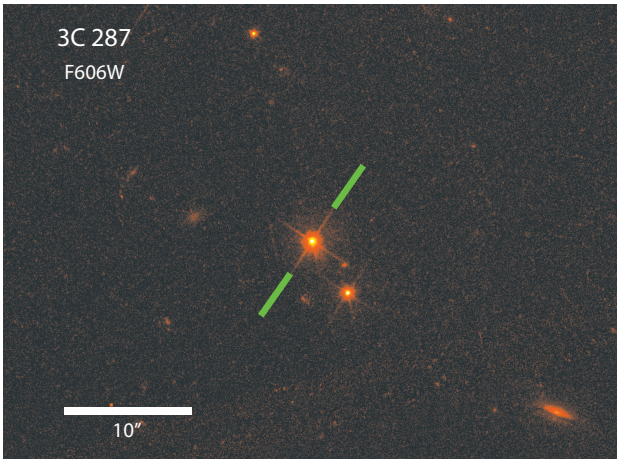

FIG. 44.— Central 35″ × 50″ of the UVIS image of QSO 3C 287. The image has been rotated so that North is up and East to the left. Green lines are placed on either side of the target to help identify its location.

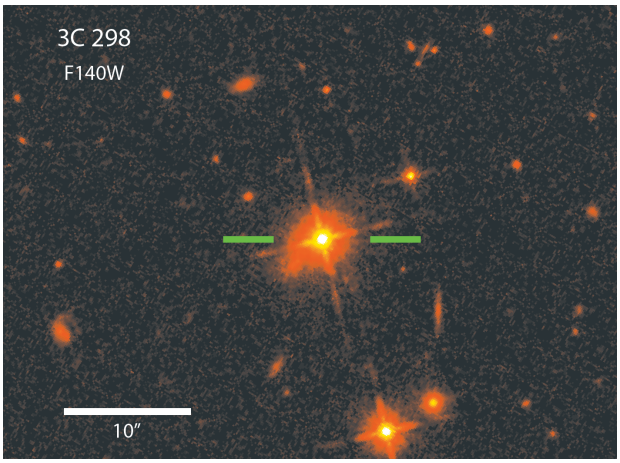

FIG. 45.— Central 35″ × 50″ of the IR image of QSO 3C 298. The image has been rotated so that North is up and East to the left. Green lines are placed on either side of the target to help identify its location.

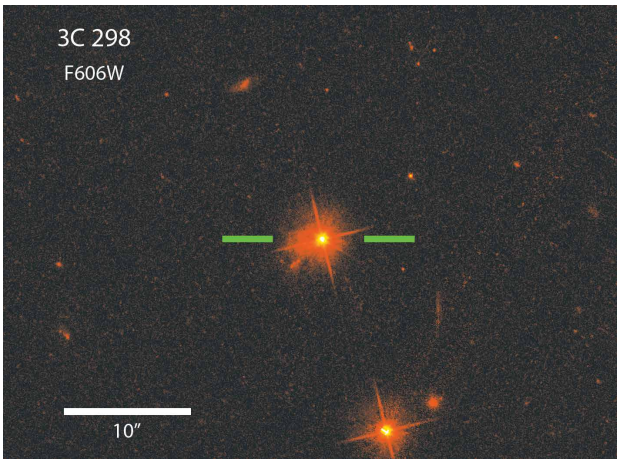

FIG. 46.— Central 35″ × 50″ of the UVIS image of QSO 3C 298. The image has been rotated so that North is up and East to the left. Green lines are placed on either side of the target to help identify its location.

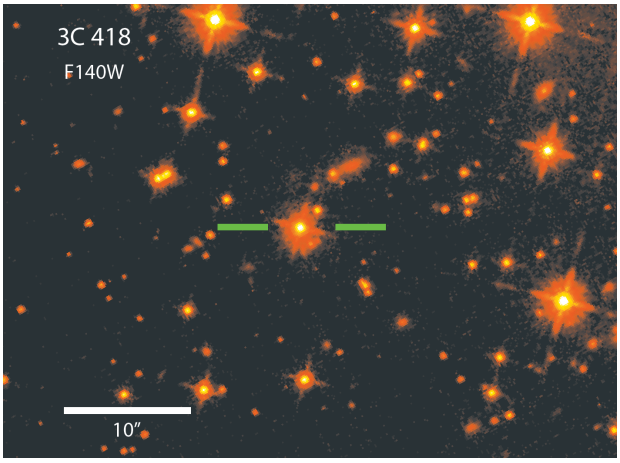

FIG. 47.— Central 35″ × 50″ of the IR image of QSO 3C 418. The image has been rotated so that North is up and East to the left. Green lines are placed on either side of the target to help identify its location.

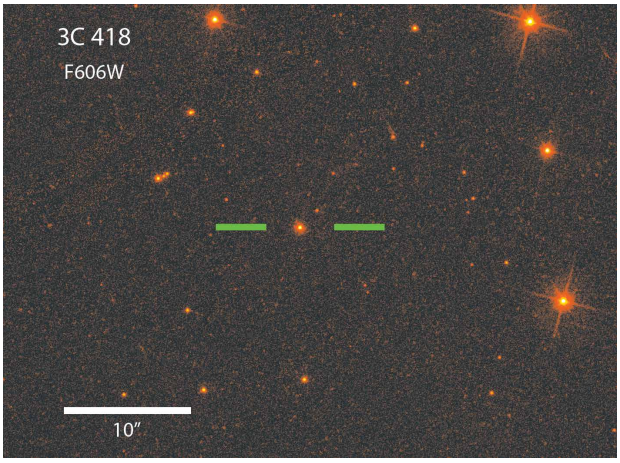

FIG. 48.— Central 35″ × 50″ of the UVIS image of QSO 3C 418. The image has been rotated so that North is up and East to the left. Green lines are placed on either side of the target to help identify its location.

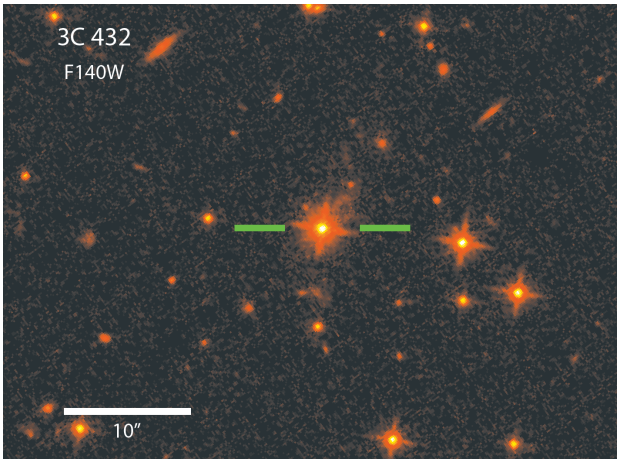

FIG. 49.— Central 35″ × 50″ of the IR image of QSO 3C 432. The image has been rotated so that North is up and East to the left. Green lines are placed on either side of the target to help identify its location.

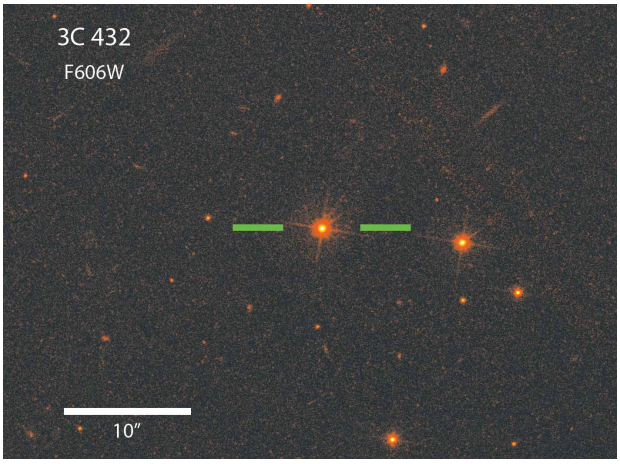

FIG. 50.— Central 35″ × 50″ of the UVIS image of QSO 3C 432. The image has been rotated so that North is up and East to the left. Green lines are placed on either side of the target to help identify its location.

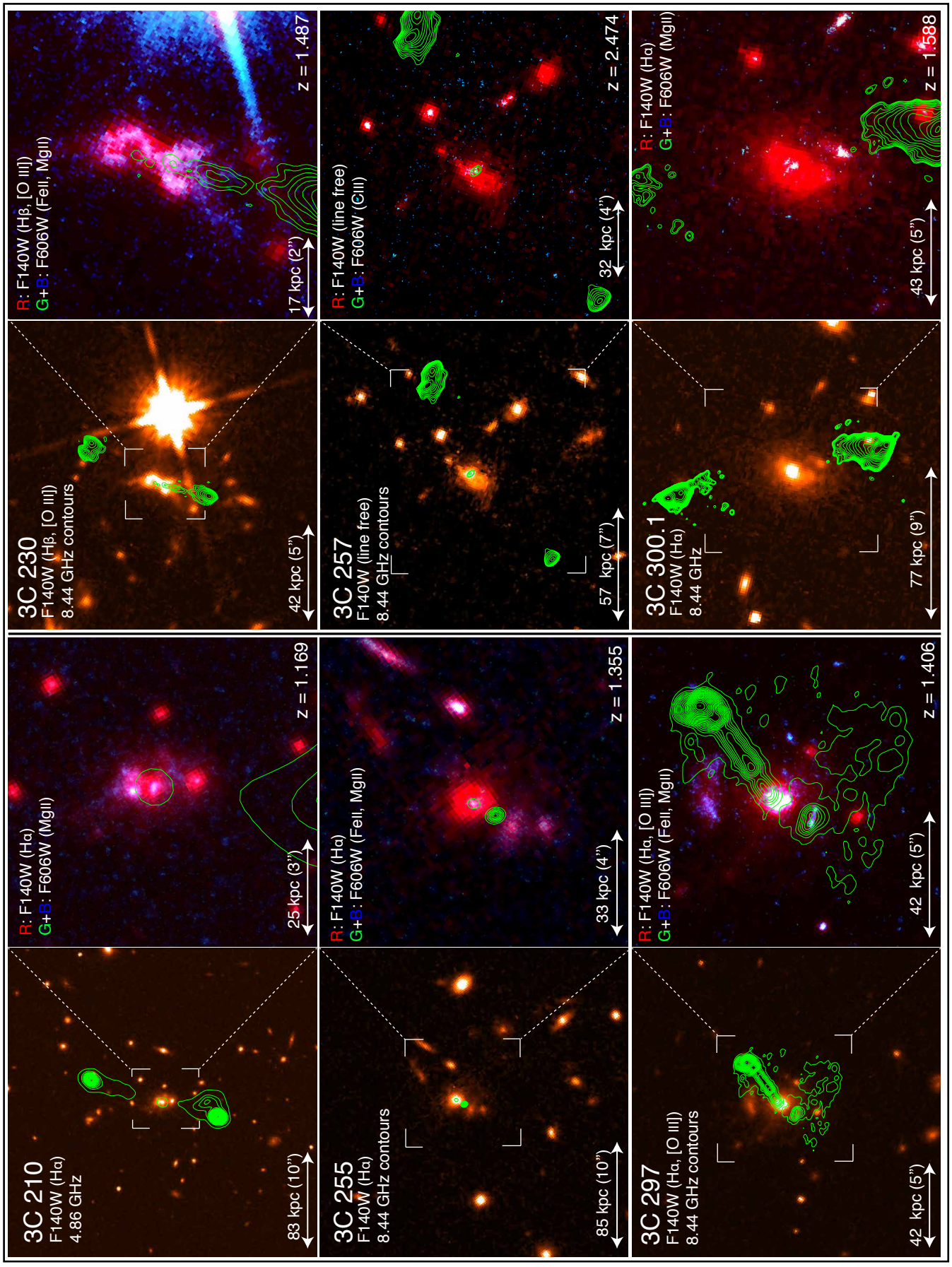

FIG. 51.— Radio galaxy optical and IR observations with overlain radio maps. The images have been rotated so that North is up and East to the left.

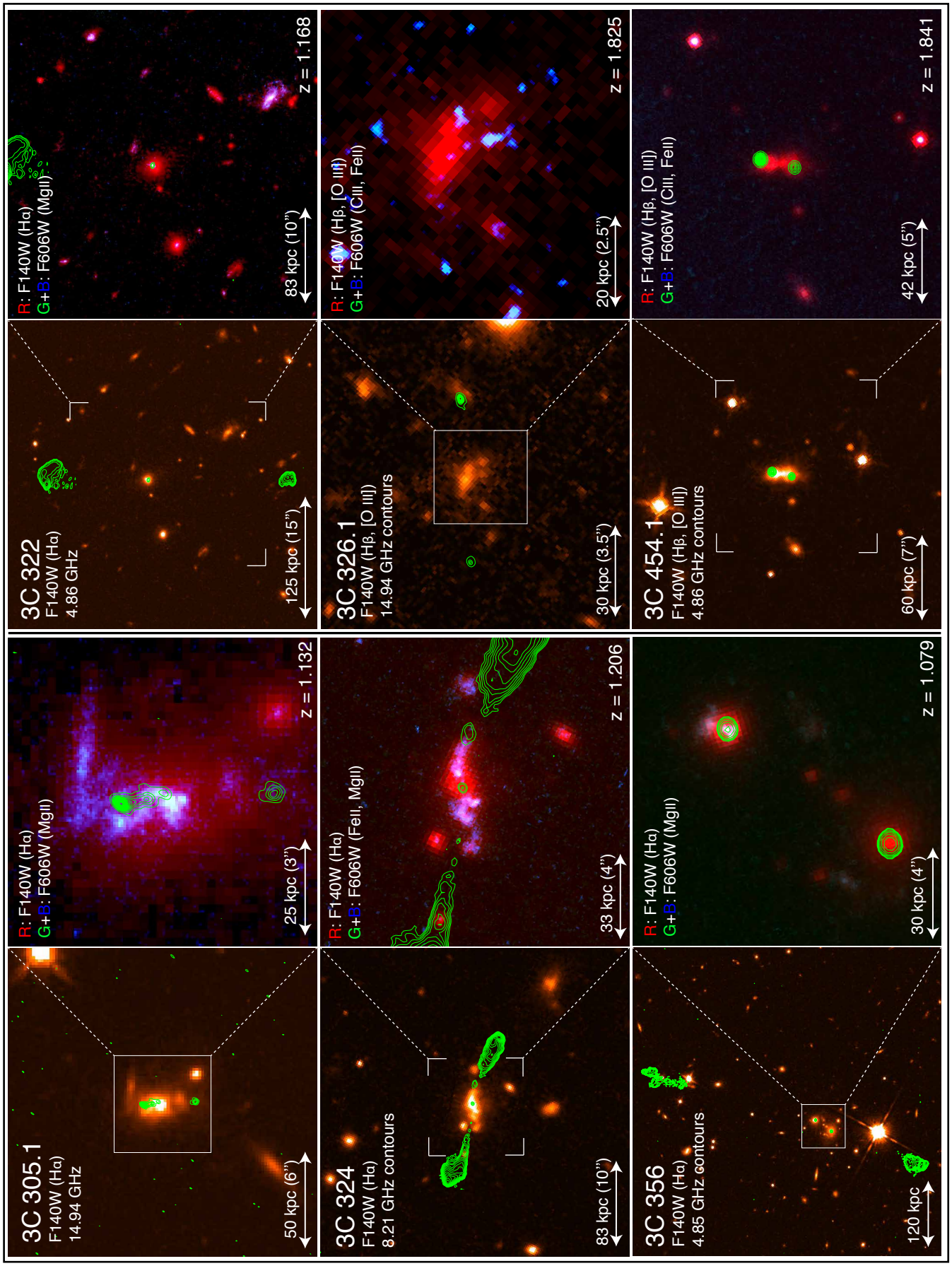

FIG. 52.— Radio galaxy optical and IR observations with overlain radio maps. The images have been rotated so that North is up and East to the left.

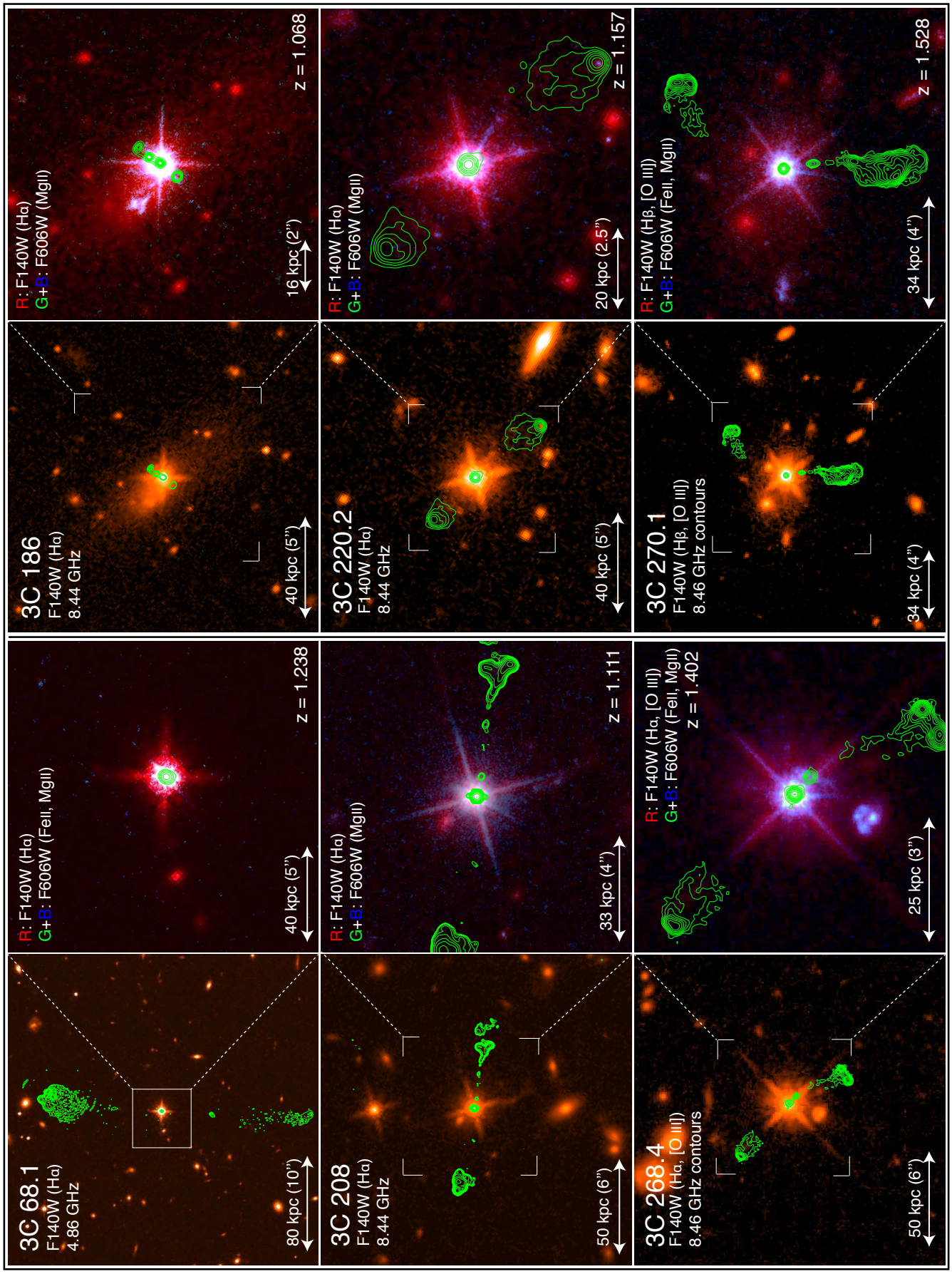

FIG. 53.— QSO optical and IR observations with overlain radio maps. The images have been rotated so that North is up and East to the left.

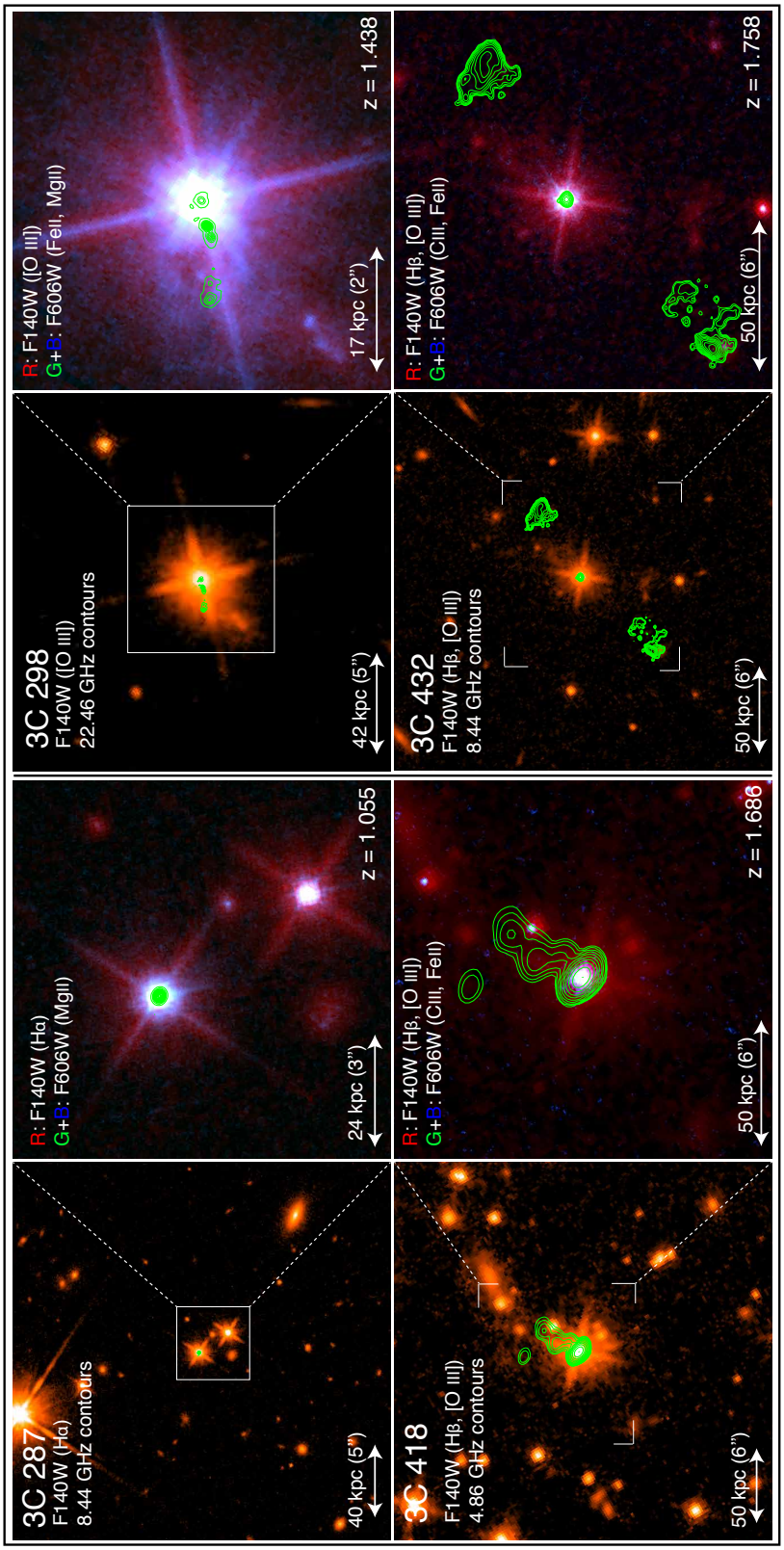

FIG. 54.— QSO optical and IR observations with overlain radio maps. The images have been rotated so that North is up and East to the left.